

Lactate-dependent transcriptional regulation controls mammalian eye morphogenesis

Received: 20 June 2022

Accepted: 26 June 2023

Published online: 14 July 2023

 Check for updates

Nozomu Takata^{1,2}, Jason M. Miska^{3,4,13}, Marc A. Morgan^{5,6,13}, Priyam Patel⁷, Leah K. Billingham³, Neha Joshi⁷, Matthew J. Schipma⁷, Zachary J. Dumar⁵, Nikita R. Joshi⁸, Alexander V. Misharin⁸, Ryan B. Embry⁷, Luciano Fiore^{1,9}, Peng Gao¹⁰, Lauren P. Diebold⁸, Gregory S. McElroy^{8,11}, Ali Shilatifard⁵, Navdeep S. Chandel^{8,12} & Guillermo Oliver¹✉

Mammalian retinal metabolism favors aerobic glycolysis. However, the role of glycolytic metabolism in retinal morphogenesis remains unknown. We report that aerobic glycolysis is necessary for the early stages of retinal development. Taking advantage of an unbiased approach that combines the use of eye organoids and single-cell RNA sequencing, we identify specific glucose transporters and glycolytic genes in retinal progenitors. Next, we determine that the optic vesicle territory of mouse embryos displays elevated levels of glycolytic activity. At the functional level, we show that removal of Glucose transporter 1 and Lactate dehydrogenase A gene activity from developing retinal progenitors arrests eye morphogenesis. Surprisingly, we uncover that lactate-mediated upregulation of key eye-field transcription factors is controlled by the epigenetic modification of histone H3 acetylation through histone deacetylase activity. Our results identify an unexpected bioenergetic independent role of lactate as a signaling molecule necessary for mammalian eye morphogenesis.

The vertebrate retina utilizes aerobic glycolysis (Warburg effect) to convert most of the glucose into lactate, even in the presence of oxygen, similar to actively growing mitotic tumor cells^{1–6}. Non-proliferative and terminally differentiated neurons in the retina are

among the most metabolically active cells in our body^{6–8}. Some of the key roles of metabolism in the retina have been described in some physiological and disease contexts^{9–11}. Although the vertebrate retina requires both glycolysis and oxidative phosphorylation to allow

¹Center for Vascular and Developmental Biology, Feinberg Cardiovascular and Renal Research Institute, Feinberg School of Medicine, Northwestern University, Chicago, IL 60611, USA. ²Simpson Querrey Institute for BioNanotechnology, Northwestern University, 303 E. Superior Street, Chicago, IL 60611, USA. ³Department of Neurological Surgery, Northwestern University Feinberg School of Medicine, Chicago, IL 60611, USA. ⁴Northwestern Medicine Malnati Brain Tumor Institute of the Lurie Comprehensive Cancer Center, Feinberg School of Medicine, Northwestern University, Chicago, IL, USA. ⁵Simpson Querrey Institute for Epigenetics and Department of Biochemistry and Molecular Genetics, Northwestern University Feinberg School of Medicine, Chicago, IL 60611, USA. ⁶Department of Oncology, St. Jude Children's Research Hospital, Memphis, TN 38105, USA. ⁷Center for Genetic Medicine, Northwestern University, Chicago, IL 60611, USA. ⁸Department of Medicine, Division of Pulmonary and Critical Care Medicine, Northwestern University, Feinberg School of Medicine, Chicago, IL 60611, USA. ⁹Laboratory of Nanomedicine, National Atomic Energy Commission (CNEA), Av. General Paz 1499, B1650KNA San Martín, Buenos Aires, Argentina. ¹⁰Robert H. Lurie Cancer Center Metabolomics Core, Northwestern University Feinberg School of Medicine, Chicago, IL 60611, USA. ¹¹Department of Ophthalmology, Duke University School of Medicine, Durham, NC 27710, USA. ¹²Department of Biochemistry and Molecular Genetics, Northwestern University Feinberg School of Medicine, Chicago, IL 60611, USA. ¹³These authors contributed equally: Jason M. Miska, Marc A. Morgan.

✉ e-mail: guillermo.oliver@northwestern.edu

functional vision initiation and maintenance, aerobic glycolysis dominates ATP production and biosynthesis even in the growing retina during development^{12–15}. However, what advantage is conferred by preferentially utilizing aerobic glycolysis in retinal tissue morphogenesis is not yet known.

Metabolic choices play a pivotal role during cell proliferation and differentiation, as metabolites support energetic demands and regulate various cellular signaling processes^{4,16–20}. Although the traditional role of aerobic glycolysis is to support biomass production and ATP during rapid cell proliferation and tissue growth⁴, recent work showed that graded glycolysis along the body axis participates in embryonic tissue patterning^{21,22}. Intriguingly, it was also shown that during chicken embryonic development, glycolysis-mediated regulation of intracellular pH is central to control a critical cellular signaling and posttranslational modifications such as acetylation during mesodermal differentiation²³. Furthermore, a recent study demonstrated that lactate, the end product of glycolysis, can act as a signaling molecule that directly marks lactylation, a novel type of histone modification necessary to regulate gene expression upon macrophage polarization^{24–30}. Aerobic glycolysis-derived lactate appears to play a vital role in introducing an additional regulatory layer to protein modifications and epigenetic control of gene expression in the context of immune responses, disease, and embryonic development^{31,32}.

The initial morphological sign of eye formation starts with the evagination of the optic vesicles (OV)^{33,34}. Similar to a variety of epithelial tissues, OV formation involves dynamic cellular movements, precise regulation of cell-cell adhesion, and cytoskeletal and extracellular matrix rearrangements^{34–38}. However, the mechanisms driving genetic and epigenetic programs during epithelial morphogenesis remain unclear. We previously demonstrated that embryonic stem cell-derived eye organoids are a valuable resource to characterize the cellular and molecular steps regulating mammalian eye morphogenesis^{39–41}. In the present study, we evaluated the functional role of aerobic glycolysis during retinal development. Using an approach that combines the use of eye organoids and single-cell RNA sequencing (sc-RNAseq) we initially identified an enrichment in glycolytic genes, including specific glucose transporters, in retina progenitor cell clusters during optic vesicle formation. Validating this finding, we found that glucose uptake was elevated in the anterior neural plate of mouse embryos, and conditional functional inactivation of the glucose transporter 1 (*Glut1*; also known as *Slc2a1*) and lactate dehydrogenase A (*Ldha*) genes displayed an impairment in eye morphogenesis. Surprisingly, addition of lactate alone to cultured eye organoids was sufficient to rescue the arrest in eye morphogenesis in cultures lacking LDH activity. Using RNA sequencing (RNA-seq) and chromatin immunoprecipitation sequencing (ChIP-seq) approaches we uncovered that lactate-mediated epigenetic modification is responsible for the upregulation of a set of key eye field transcription factors required for eye morphogenesis. These results demonstrate that lactate is a signaling molecule that plays a bioenergetics-independent role during eye morphogenesis.

Results

Glycolysis is required for optic vesicle morphogenesis in eye organoids

To better characterize the morphological and molecular steps participating in the initial process of OV and retina progenitor formation, we used eye organoids as previously described³⁹. Detailed histological and immunological comparison of early stages of OV morphogenesis using mouse embryos and mouse organoids allowed us to divide this process into four main phases (Fig. 1A–G). During phase 1 forebrain identity is acquired, in phase 2 (eye field stage³³) weak and scattered expression of *Rax*, a critical regulator of eye morphogenesis is detected, in phase 3 OV budding starts and *Rax* is more prominent and localized, and finally in phase 4 the OVs fully evaginate and enlarge

through a ballooning process and higher *Rax* expression levels are seen in the future neural retina (NR), but remain lower in the prospective retina pigment epithelium (RPE). To characterize those morphological changes in further detail we performed scRNA-seq of organoids collected prior and soon after OV evagination (phase 2 and 3, Fig. 1G). Initial bioinformatic analysis confirmed that phases 2 and 3 are transcriptionally different (Fig. 1H) and include unique cluster subtypes (Fig. 1I). These cluster subtypes were annotated using a combination of known cell fate markers identified by scRNA-seq analysis as well as genes known to be required for OV formation *in vivo*⁴². These optic vesicle and anterior neural plate cell subtypes were validated using the available mouse embryo's scRNAseq dataset^{43,44} (<https://marionilab.cruk.cam.ac.uk/MouseGastrulation2018/>).

It has been reported that glucose uptake in the developing tooth epithelia plays a crucial functional role in tissue morphogenesis, as blocking the activity of *Glut1/2* causes metaplasia of dental epithelial tissues⁴⁵. In addition, high D-glucose stimulates *Pax2* gene expression and controls ureteric bud branching morphogenesis⁴⁶. During early development, the initial glycolysis step is mediated by *Glut1/3* transport of extracellular glucose inside cells^{47,48}. Using UMAP and violin plot analysis of the scRNA-seq data we identified the expression of the two glucose transporter genes *Slc2a1* (*Glut1*) and *Slc2a3* (*Glut3*) and of the glycolytic enzyme *Ldha* in the OV and anterior neural plate subtypes (Fig. 2A). To determine whether glycolysis has any functional role during eye morphogenesis we added to the cultured eye organoids 2-deoxy-glucose (2-DG), a competitive inhibitor of glycolysis (Fig. 2B). Interestingly, 2-DG arrested OV morphogenesis, as indicated by the lack of *Rax*-GFP⁺-expressing OVs and by the reduction in the expression levels of typical eye markers such as *Rax* and *Six3* (Fig. 2C–F). We next depleted the last step of glycolysis by inhibiting LDHA activity, an enzyme involved in the generation of lactate from pyruvate and the regeneration of NAD⁺⁴⁹. Surprisingly, use of the specific chemical inhibitor GNE-140 (LDHi)⁵⁰ to block LDH activity was sufficient to mimic the phenotype observed upon glucose inhibition, resulting in an arrest in OV morphogenesis and a reduction in the expression levels of *Rax* and *Six3* (Fig. 2B, G, H). Quantification analysis further validated this observation, as the expression of the main eye field transcription factors was significantly reduced in the presence of GNE-140 (Fig. 2I). No significant toxicity produced by the addition of either 2-DG nor GNE-140 was observed (Supplementary Fig. 1A). Depletion of LDH activity after phase 2 did not show any major alteration in OV morphogenesis (Supplementary Fig. 1B). These results argue that glycolysis plays a critical role during OV morphogenesis in eye organoids.

Glut1 and *Ldha* activity are required for eye morphogenesis in mouse embryos

It has been reported that glycolysis regulates tail bud development in a region-specific fashion²¹. To evaluate the *in vivo* physiological roles of glycolysis during eye morphogenesis we first took advantage of dissected mouse embryos to monitor glucose uptake across the neural plate. To do this, we incubated wild-type (WT) embryos in eye organoid's medium (RDM) containing the fluorescent tracer 2-NBDG. Intriguingly, specific strong uptake signal was detected mostly in the presumptive OVs territory within the anterior neural plate (Fig. 3A, B). Half a day later, while the signal in the OVs remained, it was also evident in the midbrain and tail bud (Fig. 3C). Consistent with this observation, *Glut1* and *Glut3* are reported to be expressed in the presumptive OV territory, although *Glut1* expression is higher than that of *Glut3*⁵¹. It was previously described that *Glut1* null embryos have severe growth retardation and major morphological abnormalities, including the lack of visible eyes⁵². To functionally validate the activity of the glucose transporter *in vivo*, we took advantage of available *Glut1* mutant mice to evaluate whether this gene is responsible for the observed glucose uptake. As shown in Fig. 3E, glucose tracer uptake

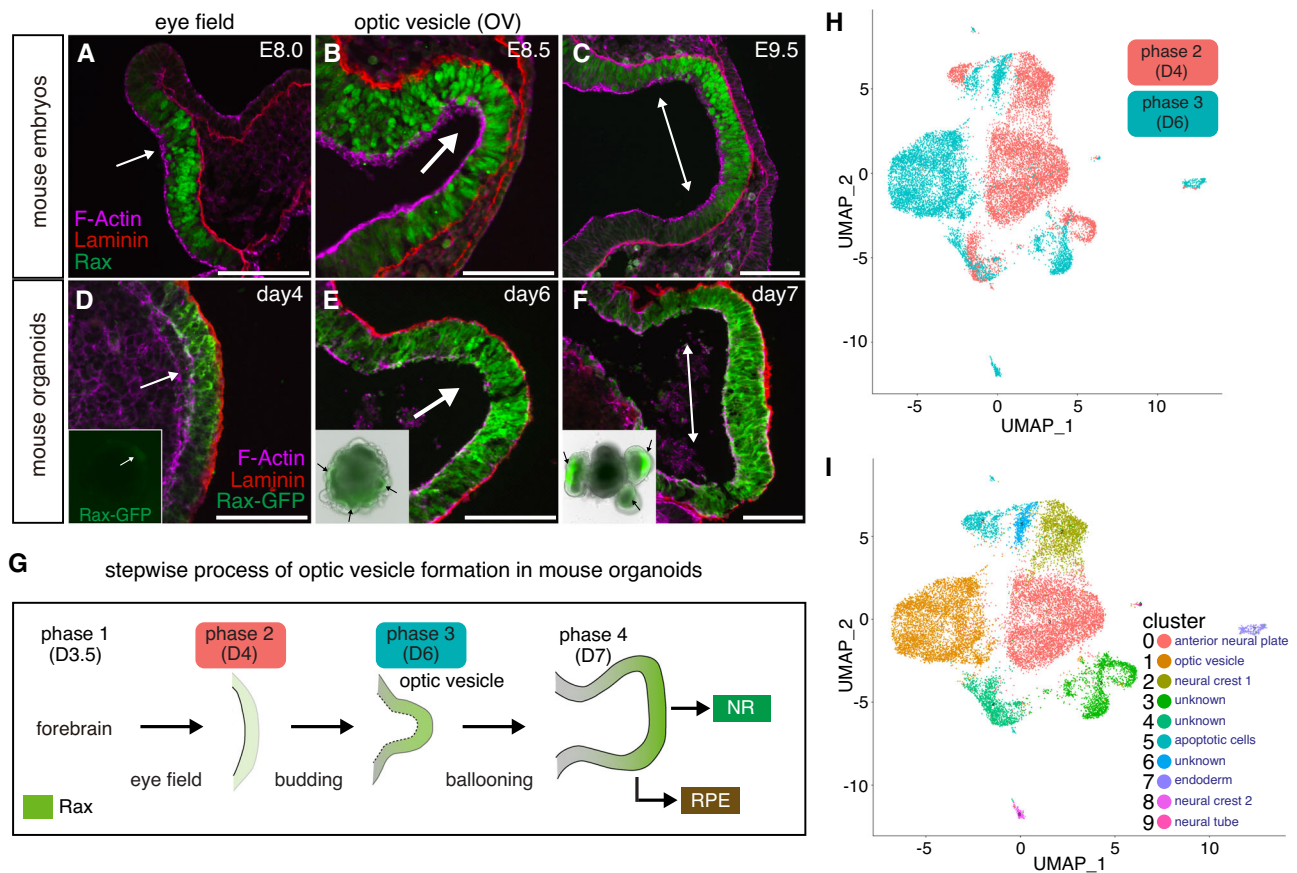


Fig. 1 | Single cell transcriptomics of mouse eye organoids during optic vesicle evagination. **A–F** Immunostaining of sections of optic vesicles from mouse embryos and eye organoids was performed using Laminin, Rax and GFP antibodies. DAPI and Phalloidin were used to label nuclei and F-actin, respectively. Insets show the merged images with bright fields and GFP channels at each embryonic and organoid stage. Black arrows in insets indicate evaginating OV. Representative micrographs are shown as similar results were obtained from three independent experiments. **G** Schematic diagram showing the processes of OV evagination in eye organoids divided into four main phases. During phase 1 (day 3.5), forebrain identity is acquired; in phase 2 (day 4), weak and scattered Rax expression starts to be detected (eye field stage); in phase 3 (day 6), OV budding starts and Rax

expression is increased; in phase 4 (day 7), through a ballooning process OVs fully evaginate and enlarge, and Rax expression is higher in the future neural retina territory (NR). Regions with lower levels of Rax expression will become the retina pigment epithelium (RPE). **H** Following single-cell RNA sequencing (scRNAseq) of the eye organoids, t-SNE plot analysis of phase 2 and phase 3 shows the obvious transcriptomic differences between these 2 stages. **I** t-SNE plot analysis shows each transcriptionally distinguishable cluster by unique colors. The bioinformatic analysis partitioned the cells of those two phases into 10 groups (clusters 0–9 are visualized using t-SNE). Each cell type is annotated based on a combination of known cell fate markers. Scale bars, 100 μm (A–F).

was impaired in the presumptive OV territory of these mutant embryos when compared with that in their heterozygous littermates (Fig. 3D). This result suggests that *Glut1* likely mediates glucose uptake in the developing eye territory. This outcome led us to question whether the eye field fate or lineage has a causal relationship with the observed glucose uptake impairment. To test this possibility, we took advantage of *Rax* and *Six3* null embryos whose rostral neural identity, including the eye field is completely missing^{53,54}. Surprisingly, we also observed a substantial reduction of the glucose tracer signals in the rostral most part of *Rax* and *Six3* mutant embryos (Fig. 3F–J). These results suggest that *Rax* and *Six3*-promoted eye identity is required for tissue-specific glucose uptake during mouse eye formation.

To conclusively evaluate whether *Glut1* activity is physiologically required during eye morphogenesis, we generated conditional null embryos using the eye field specific *Rax-Cre* mouse strain⁵⁵. Interestingly, *Glut1* conditional mutant embryos showed impaired eye structures at E8.5 (Fig. 3K, L). To characterize the mutant phenotype in further detail, we performed immunostaining using Rax and the forebrain marker *Lhx5*⁵⁶. Supporting the result discussed above, in mutant embryos Rax expression was reduced (Rax activity is

critical to induce the eye field territory and OV evagination⁵³), whereas that of *Lhx5* appears normal (Fig. 3M, N). It was recently shown that lactate production is correlated with lung branching morphogenesis, as *Ldha* displayed specific expression in a region where the distal lung buds progressively grow⁵⁷. Homozygous null *Ldha* embryos are early lethal after implantation, probably because impairing glycolysis results in the loss of the main source of ATP⁵⁸. Because of this early lethality, to impair lactate production in the eye territory we generated *Ldha;Rax-Cre* conditional null embryos. Similar to *Glut1* conditional null embryos, we found that OV formation is arrested and Rax expression is severely reduced in these mutant embryos (Fig. 3O, P). Quantification analysis performed in *Glut1;Rax-Cre* and *Ldha;Rax-Cre* conditional null embryos corroborated the significant reduction in the expression of the eye developmental marker Rax (Fig. 3Q). This reduction and the arrest in OV formation in *Glut1* mutant embryos were not as severe as in *Ldha* mutant embryos (Fig. 3L–Q). We cannot rule out the possibility that other glucose transporters in the OVs could play a compensatory role and partially restore OV morphogenesis. These results revealed that glycolysis is essential for eye morphogenesis in vivo (Fig. 3R).

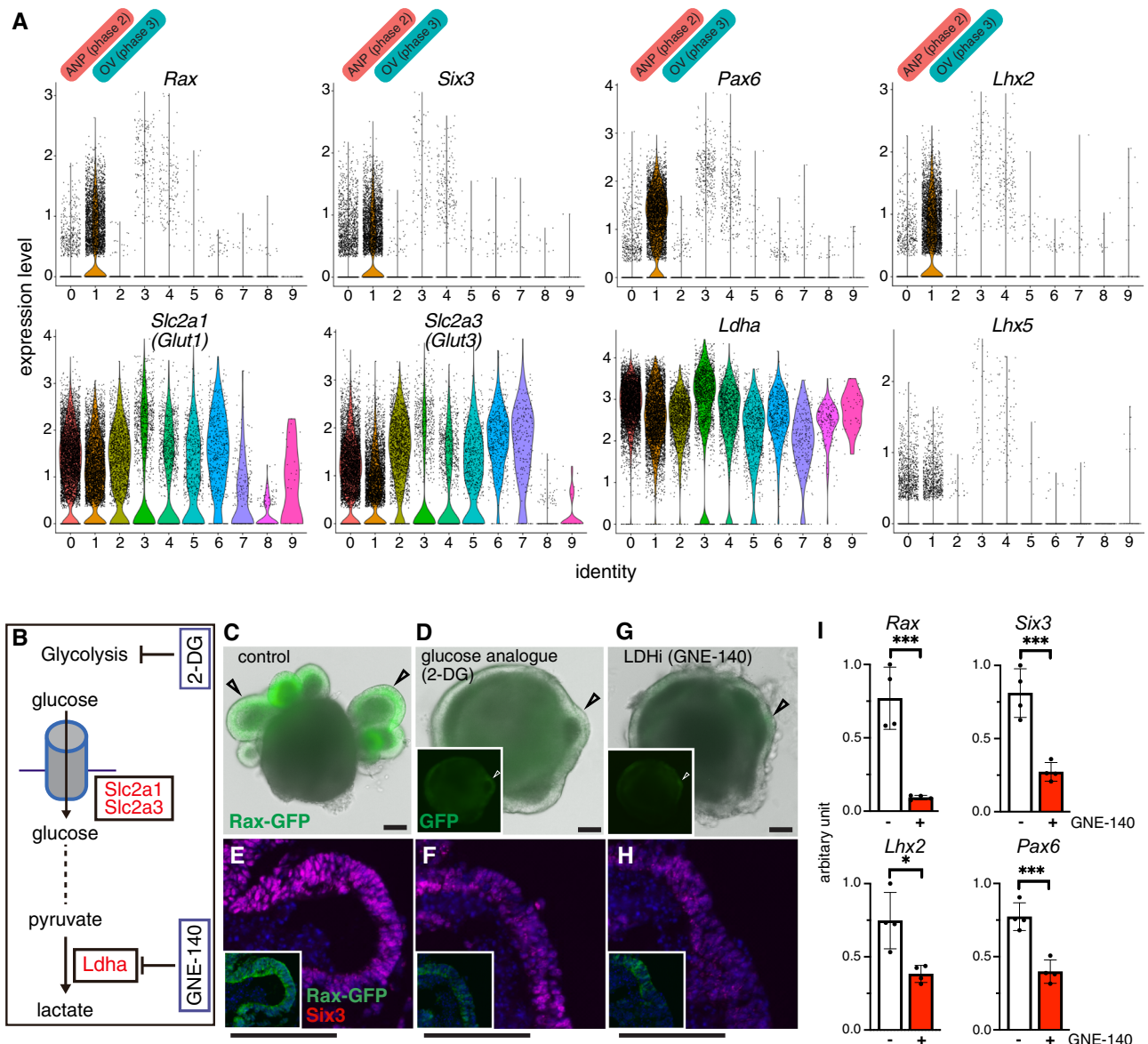


Fig. 2 | Glycolysis regulates optic vesicle morphogenesis in eye organoids.

A Violin plots identify higher expression of the early eye differentiation markers *Six3*, *Rax*, *Pax6* and *Lhx2* on cluster 1. They also express *Slc2a1 (Glut1)*, *Slc2a3 (Glut3)* and *Ldha*. *Lhx5* is a forebrain marker. **B–H** Pharmacological inhibition of glucose catabolism and LDH activity by 2-Deoxy-d-Glucose, 2-DG (2 mM) and GNE-140 (20 μ M) respectively, shows that formation of *RaxGFP*⁺-expressing OV (arrow-heads) is arrested and the expression levels of eye markers such as *Rax* and *Six3* is severely reduced (**E, F, H**). Insets indicate *Rax-GFP* expression (**D–H**).

Representative micrographs are shown as similar results were obtained from three independent experiments (**C–H**). **I** Quantitative PCR analysis of a set of key eye field transcription factors known to be necessary during the process of eye morphogenesis. Scale bars, 100 μ m (**C–H**). Unpaired Student's *t* test (two-tailed) was performed (**I**). * or *** indicates a *p*-value is less than 0.05, or 0.001, respectively (**I**). Data are presented as mean values \pm SEM (**I**). Source data are provided as a Source Data file. *n* = 3 biologically independent experiments were performed.

Fate tracing of glucose identified elevated lactate levels in eye organoids

To characterize glycolysis-derived metabolites that might participate in eye morphogenesis we used a glucose fate-tracing approach. Glucose is catabolized by glycolysis to pyruvate that can be converted into alanine, lactate or enter mitochondria⁵⁹. Glucose can also enter multiple branched pathways from glycolysis including the hexosamine, pentose phosphate, and de novo serine biosynthetic pathways⁵⁹. To identify the endogenous biochemical cascade in OV progenitor cells, we performed a direct quantification of glucose consumption using ¹³C-glucose tracing experiments followed by liquid chromatography–mass spectrometry (LC-MS/MS) analysis to profile downstream metabolites and their dynamics inside a cell⁶⁰. A major analytical challenge with this procedure is the amount of

material that can be obtained per embryo, and the certainty that they are all at the correct developmental stage. To avoid this problem, we took advantage of the eye organoids to pool 50 organoids per time point and/or condition. Because the natural abundance of isotopic metabolites in the early eye organoids has not yet been reported, we have initially performed LC-MS/MS without exogenous isotopic labeling to show the natural abundance of isotopic carbons. The natural abundance of *M* + 1 isotopologues was less than 5% for every metabolite measured, whereas for the *M* + 2/4 TCA cycle and other glycolytic intermediates it was essentially 0. For any higher-order labeling more than *M* + 2, natural abundance was undetectable in most metabolites (Supplementary Fig. 2A, B). The exception was the natural abundance of *M* + 3 labeled lactate that is approximately 4% (the average 3.97 SEM \pm 2.00%, Supplementary Fig. 2B). Next, eye

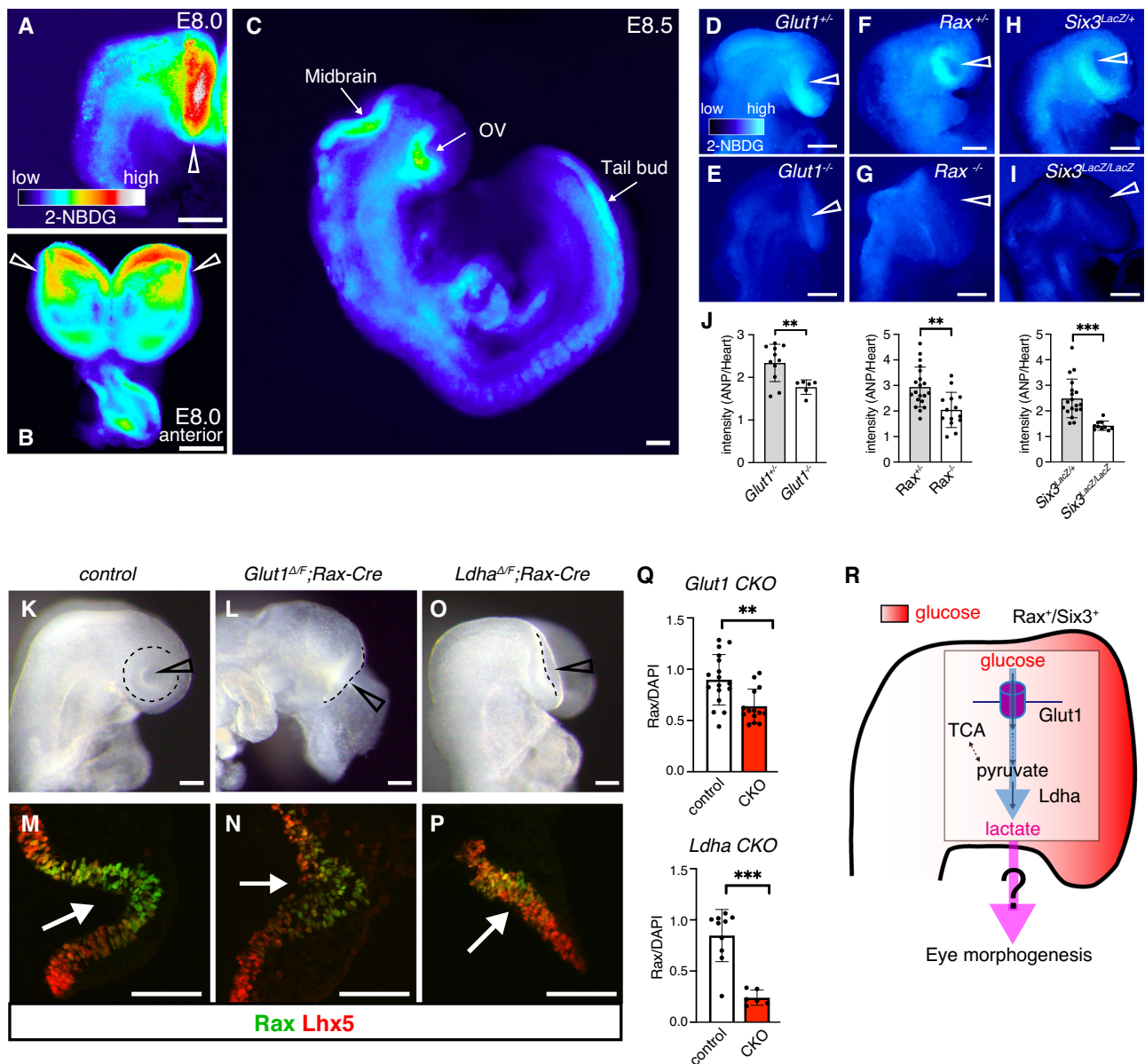


Fig. 3 | Active glucose uptake takes place in the eye field territory of mouse embryos. **A–C** A strong glucose uptake signal was initially detected mostly in the presumptive OV_s at E8.0 (arrowheads), and in the midbrain and tail bud region at the 5–6 somite stage (E8.5). Representative micrographs are shown as similar results were obtained from three independent experiments. **D–I** Glucose tracer uptake was impaired in the presumptive OV territory of *Glut1*, *Rax* and *Six3* mutant embryos compared with that in their heterozygous littermates. **J** Quantification of 2-NBDG fluorescence intensity in those embryos. 2-NBDG intensity in the anterior neural plate (ANP) was measured relative to the heart primordium. **K–P** Bright field images and immunostaining showing that OV morphogenesis in *Glut1* and *Ldha*

conditional null embryos was impaired. *Rax* expression was reduced, while expression of the forebrain marker *Lhx5* was not dramatically affected in those mutant embryos. The Delta allele was generated by germline deletion using *Ella-Cre mice*. Only one flox allele remains upon conditional Cre expression. **Q** Quantification of *Rax* expression relative to DAPI signals. **R** Schematic representation of the glycolysis process during eye morphogenesis. Scale bars, 100 μ m (**A–I**, **K–P**). Unpaired Student's *t* test (two-tailed) was performed (**J**, **Q**). ** or *** indicates a *p*-value is less than 0.01 or 0.001, respectively (**J**, **Q**). Data are presented as mean values \pm SEM (**J**, **Q**). Source data are provided as a Source Data file. *n* = 3 biologically independent experiments were performed.

organoids were cultured in medium containing uniformly labeled ^{13}C -glucose, and the label propagation in glycolytic metabolites was measured at several time points within the first 120 min after the addition of ^{13}C glucose. Amongst all detected glycolytic intermediates, the majority of ^{13}C glucose-derivatives was lactate, while citrate, one of the signature metabolites of the TCA cycle exhibited extremely low levels over the entire labeling measurement (Fig. 4A). Intriguingly, half of the glycolytic lactate became labeled in the first 15 min and saturated up to 80% (Fig. 4A). By contrast, citrate in the TCA cycle took 1 h to reach steady state, wherein only about 20% of the citrate pool was ^{13}C labeled (Fig. 4A). As shown in Fig. 4B, labeling

was reduced in TCA cycle metabolites as the cycle progressed, while pyruvate production reached more than 90% (Supplementary Fig. 3A). This initial isotopic labeling analysis indicates less activity of the TCA cycle in the eye organoids. It is also important to collect all the intermediate metabolites over the given period during the time-course analysis, as the TCA cycle undergoes multiple rounds^{61,62}. Thus, we also measured M4, M5, M6 of TCA cycle metabolites and pyruvate carboxylase mediated M1 and M3 labeled metabolites. However, as the labeling through the TCA cycle is limited in these organoids (Fig. 4B and Supplementary Fig. 3B), we observed little to no labeling of M + 4 intermediates, indicating that over two hours

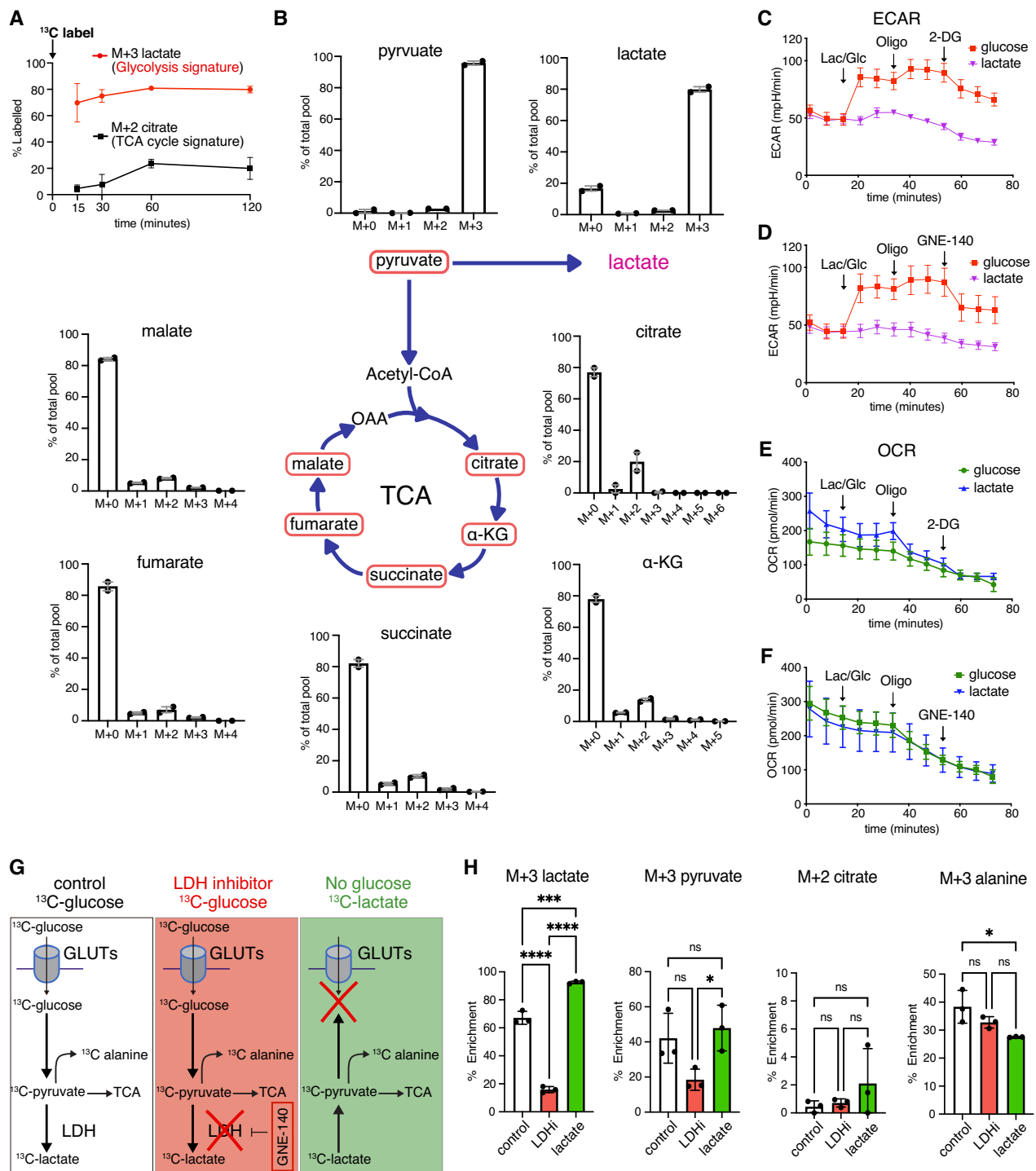


Fig. 4 | ¹³C-isotope labeling reveals the profile of glycolytic intermediates during eye morphogenesis. **A, B** The direct quantification of glucose consumption using ¹³C glucose time-course tracing was performed in cultured eye organoids and measured by LC-MS/MS analysis. Amongst all detected glycolytic intermediates, the main ¹³C glucose-derivatives were pyruvate and lactate, while the levels of citrate, one of the signature metabolites of the TCA cycle were extremely low. The M + 0, M + 1, M + 2 and M + 3 metabolites were measured as % of the total pool to distinguish unlabeled and labeled metabolites. The labeled lactate during glycolysis saturated up to 80%. In the TCA cycle, citrate shows that only about 20% of the succinate pool was ¹³C labeled. **C–F** To evaluate glycolysis and mitochondrial respiration, seahorse analysis was performed to measure eye organoids-derived extracellular acidification rate (ECAR) and oxygen consumption rate (OCR). Injecting glucose (Glu) elevated ECAR whereas lactate (Lac) did not. Oligomycin

(Oligo), an inhibitor of ATP synthase necessary for oxidative phosphorylation further increased ECAR levels. Subsequent addition of either 2-DG or GNE-140 depleted the ECAR to the basal level. **G, H** ¹³C-glucose labeling under three conditions: ¹³C-glucose = control (white scheme), ¹³C-glucose + LDHi = LDHi (red scheme), ¹³C-lactate in glucose free media mimicking the lack of glucose uptake = lactate (green scheme). Treatment with LDHi (which prevents OV morphogenesis) significantly reduced ¹³C-labeled lactate; however, it did not change the levels of pyruvate, citrate and alanine. ¹³C-lactate was not dramatically metabolized into TCA cycle specific metabolites as seen in M + 2 citrate. One-way ANOVA followed by Tukey's post-hoc test was performed (**H**). *****p* < 0.0001, ****p* < 0.001, **p* < 0.05, n.s. not significant (**H**). Data are presented as mean values ± SEM (**H**). Source data are provided as a Source Data file. *n* = 3 biologically independent experiments were performed.

only one turn of the TCA cycle occurred. Regarding other intermediates, we found no detectable M + 1,3,5 labeling indicating that pyruvate carboxylase activity in these organoids was negligible. Critically, unlike LDH inhibition, functional inhibition of the mitochondrial pyruvate transporter (MPC) by UK5099⁶³ did not prevent *Rax* expression (Supplementary Fig. 3C, D).

To further evaluate glycolysis and mitochondrial respiration, Seahorse analysis was performed to measure eye organoids-derived extracellular acidification rate (ECAR) and oxygen consumption rate (OCR). We observed that as expected, glucose administration increased ECAR which was further increased with oligomycin treatment that blocks the mitochondria electron transport process (Fig. 4C, D). Treatment with either 2-DG or LDHi significantly reduced ECAR (Fig. 4C, D). It is worth noting that addition of lactate, the final glycolysis product, did not show any noticeable change of ECAR, which explains the dynamic change in acidity originated mainly from glycolysis through the initial metabolite source, glucose. By striking contrast, OCR did not show any significant difference between glucose and lactate addition (Fig. 4E, F). Furthermore, the addition of either glucose or lactate had no influence on OCR, indicating a minimal use of these substrates for TCA metabolism. This metabolite profiling and the results from the functional ablation of MPC strongly suggest that glucose in OV progenitors is preferentially metabolized into lactate rather than into TCA metabolism. Collectively, it is possible that glucose-derived lactate functionally participates in eye developmental programs.

As stated above, glucose can be fated into multiple branched signaling pathways. To examine the potential involvement of all the metabolites detected in the initial time-course tracing analysis, we performed ¹³C-glucose labeling under three conditions: ¹³C-glucose medium (control), ¹³C-glucose + LDHi medium (LDHi) and ¹³C-lactate in glucose-free medium (lactate) (Fig. 4G). Because the activity of LDHA is required for lactate production, the addition of its inhibitor significantly reduced M + 3 lactate (Fig. 4H). As expected, lactate was detected by the exogenously added ¹³C-lactate in the absence of exogenous glucose (Fig. 4H). On one hand, the TCA metabolites citrate and succinate did not change significantly by blocking LDH activity (Fig. 4H and Supplementary Fig. 4A). The result agrees with the proposal that TCA metabolites are unlikely to participate in the active process of OV morphogenesis. However, another possibility could be that alanine, which is further metabolized from pyruvate and was ¹³C-labeled in our assay (Supplementary Fig. 3E), also participates in the process of eye morphogenesis⁶⁴. However, this alternative was not validated by our assay showing that depletion of LDH activity did not cause any reduction in ¹³C-labeled alanine (Fig. 4H). Importantly, LDH depletion or ¹³C-lactate addition also failed to reduce or rescue M + 3 glycerate labeling, respectively (Supplementary Figs. 3E and 4B). Lastly, LDH inhibition had no effect on nucleotide synthesis and ¹³C-lactate labeling failed to rescue nucleotide labeling in the absence of glucose (Supplementary Fig. 4C), suggesting that OV morphogenesis is independent of the pentose-phosphate pathway. In summary, this analysis demonstrates that lactate likely plays a direct role in OV morphogenesis.

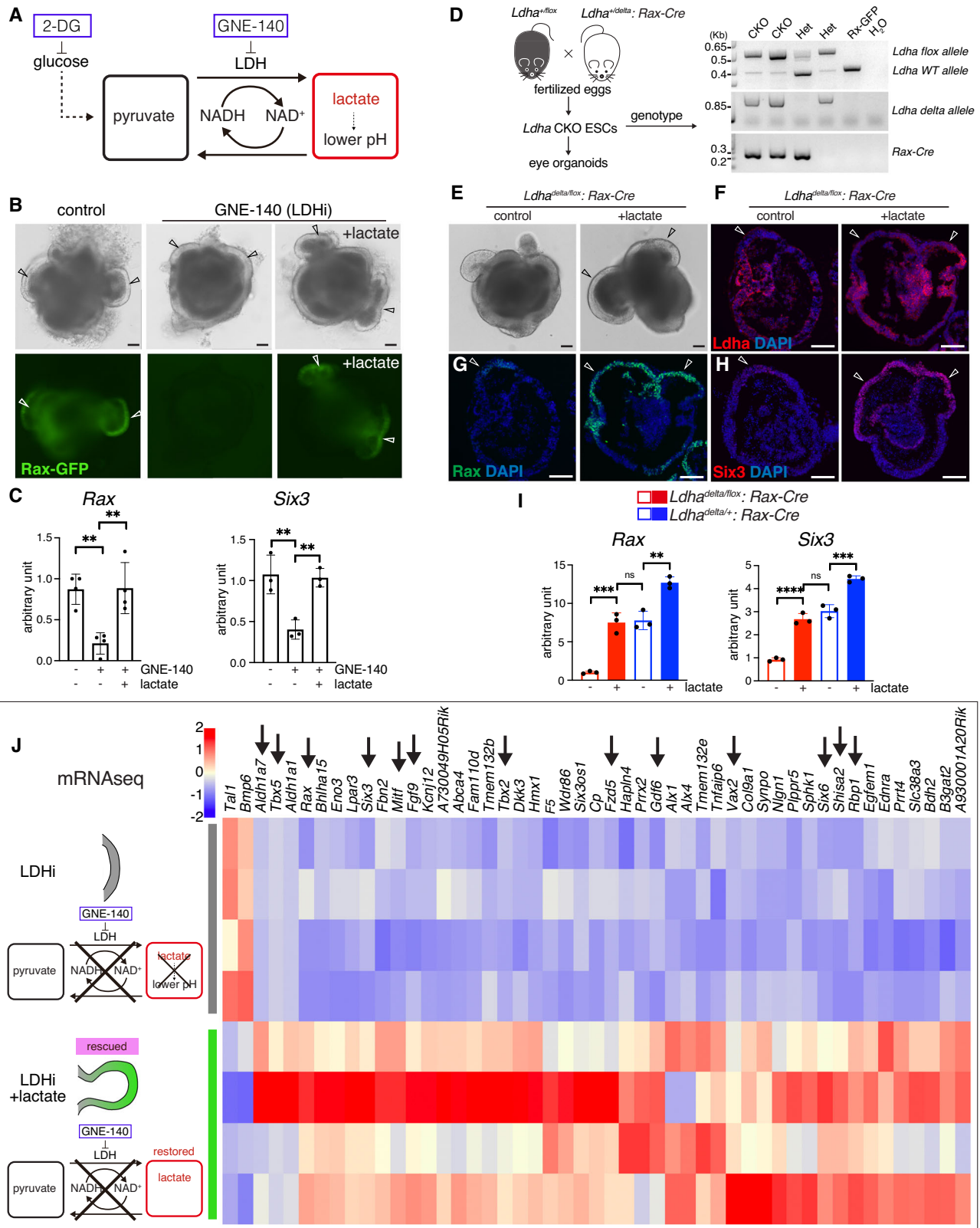
Lactate mediates eye morphogenesis

LDH activity has multiple roles in the glucose pathway, including the production of lactate that can be converted back into pyruvate⁶⁵. As seen in Fig. 4H, isotopic labeling analysis showed that pyruvate was converted from exogenous ¹³C lactate. Accordingly, we evaluated whether pyruvate could rescue the loss of OV morphogenesis caused by the addition of the LDH chemical inhibitor GNE-140 (Supplementary Fig. 5A). To facilitate pyruvate incorporation inside the cells, we added a membrane-permeable form of pyruvate⁶⁶ to the eye organoids in the presence of GNE-140. However, no noticeable rescue was

observed by the addition of methyl-pyruvate (Supplementary Fig. 5B, C). It has been reported that glycolysis-produced lactate plays a pivotal role in pH modulation during mesodermal differentiation in tail bud development²³. To test whether pH controls eye morphogenesis, we used media that changes pH in a graded fashion in the presence of the LDH inhibitor. Intracellular pH (pHi) responds to changes in extracellular pH (pHe) when a cell re-balances transmembrane acid-base fluxes that alters steady-state pHi⁶⁷. Unlike the mechanism in tail bud development, lowering the pH did not show any noticeable change in OV morphogenesis and did not rescue *Rax* expression levels (Supplementary Fig. 5D, E). Next, we tested if lactate itself could rescue the eye defects. Surprisingly, addition of sodium L-lactate, which does not change the pH, significantly rescued the defect in eye morphogenesis in the presence of either 2-Deoxy-D-glucose or GNE-140 (Fig. 5A, B and Supplementary Fig. 5F, G). Quantification analysis using qPCR confirmed that *Rax* and *Six3* expression is also rescued by the addition of lactate (Fig. 5C). To further validate this important observation in vivo we took advantage of our organoid system⁴¹ to genetically delete *Ldha* in the anterior neural plate. *Ldha*^{lox/delta};*Rax-Cre* blastocysts were used to isolate ESCs for the eye organoid differentiation assay (Fig. 5D and Supplementary Fig. 6A). Initially, day 3 *Ldha* CKO organoids expressed *Ldha* in the surrounding neural ring (Supplementary Fig. 6B). By day 7, *Ldha* CKO organoids exhibited successful deletion of LDHA expression in *Rax*-expressing cells; LDHA expression remained in heterozygous organoids (Supplementary Fig. 6C). As expected, in the mutant organoids expression of the developmental eye markers *Rax* and *Six3* was reduced significantly, while that of the pan-neural marker *Sox2* was not affected (Supplementary Fig. 6D). Next, we found that lactate addition was sufficient to rescue the OV defects in the CKO organoids (Fig. 5D–F) and as expected, expression of typical eye developmental markers was elevated (Fig. 5G–I).

Lactate drives transcriptional programs for tissue morphogenesis

Lactate production can regulate a wide variety of biological processes, including angiogenesis, hypoxia, and immune cell function^{68–70}. However, little is known about its possible transcriptional impact on signaling pathways regulating tissue morphogenesis. To identify lactate-driven transcriptomic regulation we performed RNA-seq comparing control organoids vs LDHi treated organoids and LDHi treated vs LDHi treated plus lactate (condition that rescues the OV defect). To identify lactate-dependent transcriptional changes, we initially performed a direct comparison with (LDHi+lactate) or without (LDHi) lactate. Surprisingly, heatmap representation revealed that addition of lactate resulted in significant transcriptional changes, including that of various genes known to be necessary for eye morphogenesis (Fig. 5J). Intriguingly, the eye field transcriptional factors *Six3*⁷¹ and *Rax*⁵³ were both upregulated by lactate concomitant with the rescue in eye formation. Furthermore, we identified upregulation of additional genes known to regulate eye morphogenesis such as *Fzd5*, *Shisa2*, *Tbx2* and *Pax2* whose expression changed dramatically upon functional depletion of *Ldha* and lactate addition (Fig. 5J). As shown previously, *Fzd5* mutant mice failed to complete optic cup morphogenesis⁷². *Shisa2* loss of function or overexpression in *Xenopus* induces small eyes or ectopic eyes, respectively⁷³. Loss of *Tbx2* causes a delay in OV morphogenesis leading to small and abnormally shaped optic cups⁷⁴. *Pax2* mutations and loss of function are associated with coloboma or microphthalmia, both of which are consequences of eye morphogenesis defects^{75,76}. Changes in the expression of various other genes known to participate in different steps of eye morphogenesis are indicated by arrows in the heatmap (e.g., *Mitf*, *Fgf9*, *Aldh1a7*, *Gdf6*, *Rbp1*, *Tbx5*, *Six6* and *Vax2*) (Fig. 5J)^{77–84}. These findings allow us to conclude that glycolysis-derived lactate plays a central functional role in bridging a genetic program with eye morphogenesis.



Global profiling of epigenetic modifications by glycolysis-derived lactate

Metabolites regulate epigenetic modifications to control gene expression and cell differentiation^{85,86}. Histone acetylation is generally associated with active transcription⁸⁷. However, whether glycolysis-derived metabolites mediate epigenetic modifications important during organ morphogenesis in general, or eye development in

particular has not yet been shown. To determine whether lactate participates in epigenetic regulation required for eye morphogenesis, we performed global ChIP-seq across the genome. It is widely known that lysine 27 acetylation of histone H3 (H3K27ac) is a histone marker enriched at promoters and enhancers. Accordingly, we used a well-characterized antibody recognizing H3K27ac in chromatin isolated from eye organoids cultured with and without addition of the LDHA

Fig. 5 | Lactate is required for eye morphogenesis by regulating eye transcriptional programs. **A, B** The addition of sodium L-lactate, which does not change the pH, significantly rescued the OV phenotype (arrowheads) in the presence of 20 μ M GNE-140 (LDHi). **C** Quantification analysis using RT-qPCR confirmed that *Rax* and *Six3* expression were also rescued by the addition of sodium L-lactate (25 mM). **D** Generation and genotyping of *Ldha*^{delta/flox}; *Rax-Cre* conditional mouse embryos (CKO) and derivation of ESCs. The delta allele was generated by germline deletion using *Ella-Cre* mice. Only one flox allele remains upon conditional Cre expression. Representative micrographs are shown as similar results were obtained from three independent experiments. **E** Genetic deletion of LDHA in the eye field-specific region leads to defects in optic vesicle formation in *Ldha* mutant organoids. The addition of lactate rescued the eye defects as indicated by the formation

of OVs (arrowheads). **F–I** Immunostaining and RT-qPCR analyses showed that *Ldha*-depleted organoids recovered *Rax* and *Six3* expression in the presence of 25 mM lactate (arrowheads); however, *Ldha* expression in the mutant OVs is not detected (**F**). **J** RNA-sequencing was performed to compare LDH block (LDHi) vs LDHi plus sodium L-lactate. Addition of lactate resulted in significant transcriptional changes as indicated by heatmap analysis that identified changes in the expression of various genes known to regulate eye formation (arrows). Scale bars, 100 μ m (**B, E–H**). One-way ANOVA followed by Tukey's post-hoc test was performed (**C, I**). **** $p < 0.0001$, *** $p < 0.001$, ** $p < 0.01$, n.s. not significant (**C, I**). Data are presented as mean values \pm SEM (**C, I**). Source data are provided as a Source Data file. $n = 3$ biologically independent experiments were performed.

inhibitor. Bioinformatic analysis identified differential peaks close to gene regulatory regions. To facilitate narrowing the putative candidate genes we cross-compared the ChIP-seq and identified 414 lactate dependent genes from our RNA-seq (Fig. 6A–C). The ChIP-seq occupancy analysis determined that whereas overall genome wide H3K27ac patterns were unaffected, there was a specific loss of H3K27ac at key eye morphogenesis genes in response to LDHi (Fig. 6C, D and Supplementary Fig. 7A, B). This striking result implicates lactate as a specific key regulator involved in H3K27ac at eye developmental loci.

To explore the direct role of lactate in the eye developmental program, we sought to find potential links between lactate and histone epigenetic modifiers, such as the Histone H3 acetylation writers and erasers whose specific epigenetic activities are pivotal for normal development and disease^{88–91}. The writers, CBP and p300 act as transcription coactivators by interacting with a variety of specific transcription factors and co-regulators⁹². Standard null p300 mutant embryos show severe head defects with small eyes⁹³. CBP and p300 are required for rod and cone photoreceptor neurons and lens induction^{94–96}, suggesting CBP/p300-mediated cell fate control is important for eye development. By contrast, for one of the erasers, *Hdac1*-null embryos displayed numerous defects including severe head abnormalities leading to embryonic lethality before E9.5⁹⁷. *Hdac1* and *Hdac2* are implicated in early neural development as *Nestin-Cre* mediated conditional deletion of those two genes caused severe brain defect⁹⁸. *Hdac3* null embryos die before E9.5 due to defects in gastrulation⁹⁹. Accordingly, HDACs play important roles in early embryogenesis, including brain morphogenesis. Interestingly, a previous report demonstrated that lactate is an endogenous inhibitor of histone deacetylase activity¹⁰⁰. To seek the link between lactate and HDACs, we performed gene expression analysis of eye organoids and observed that LDHi mediated downregulation of key eye developmental genes, such as *Rax* and *Six3*, was rescued by the chemical inhibitor Panobinostat, a compound known to inhibit HDAC activity^{101,102} (Fig. 6E, F). Notably, this effect is specific to eye genes as the pan-neural marker *Sox2* was unaffected (Fig. 6E). This result provides a direct link between histone acetylation and the eye developmental program. To further dissect this link, we used a well-characterized CBP/p300 acetyltransferase inhibitor (A-485). The addition of A-485 resulted in specific downregulation of eye-determining factors (Supplementary Fig. 8A, B). The result identified the histone acetylation writer CBP/p300 as a crucial factor involved in the specific regulation of eye development. These lines of evidence suggest that the role of lactate could be to inhibit HDAC enzymatic activity, presenting a direct link between histone acetylation and the eye developmental program. Altogether, we propose that glycolysis-produced lactate in the anterior neural plate controls eye morphogenesis at the epigenetic level through histone deacetylase (Hdac) activity (Fig. 7).

Discussion

Using a combination of eye organoids and mouse genetics we now report that: a) scRNA-seq from eye organoids identified key glycolytic

genes expressed in developing OVs; b) the eye field territory of mouse embryos displays elevated glycolytic activity; c) lactate production is required for OV morphogenesis; d) glycolysis-mediated lactate upregulates eye field transcription factors and associated epigenetic modifications (H3K27ac). Together, these results identified an unexpected functional role of aerobic glycolysis during mammalian organogenesis (Fig. 7). Our data argue that lactate acts as a signaling molecule playing diverse physiological roles during organ morphogenesis.

Metabolic signals dictate cell fate and cell morphology by contributing to transcriptional programming, epigenetic modifications, and biochemical differentiation cues¹⁰³. For example, glycolysis is important for physiological wound healing in the skin through upregulation of *Glut1* and related glycolytic enzymes¹⁰⁴. The RNA-binding protein Lin28-mediated translation of gene products in glycolysis facilitates skin tissue repair by reprogramming cellular bioenergetics¹⁰⁵. In the adult stage, LDH and lactate are well-known biomarkers of a variety of tissue injuries, also presenting critical functional activity, for instance for neural regeneration post-spinal cord injury^{65,106–109}. These few reports suggest that glycolysis might play a variety of roles in tissue repair and wound healing processes. Our metabolomic and transcriptomic analysis indicate that there is a crosstalk between metabolism and tissue morphogenetic programs, leading to the possibility that metabolic regulation of cellular signaling is reused in tissue repair or remodeling processes. Future investigations may focus on glycolysis-mediated tissue repair and regeneration in a variety of embryonic and adult cell types.

In relation to lactate-mediated regulation of protein acetylation, it has been shown that glycolysis creates favorable chemical conditions for acetylation of the signaling molecule β -catenin that is important for tail bud development²³. This protein acetylation mechanism is likely conserved across vertebrate developmental programs including humans. Conversely, protein deacetylation in the nucleus is regulated by HDAC family members, which target a variety of histones, particularly histone H3. Our results demonstrate that lactate, a putative HDAC inhibitor, regulates local histone acetylation associated with the specific eye developmental program. These findings raise several exciting future directions for the study of metabolites-dependent regulation of HDAC activity in eye morphogenesis.

It was recently reported that endogenous elevation of lactate to ~ 15 mM preceded the timed degradation of cyclin B1 and securin, and mitotic exit¹¹⁰. Accumulation of intracellular lactate prior to mitosis coincided with stable expression of major enzymes that regulate pyruvate utilization¹¹⁰, and importantly no detectable proteome-wide evidence for protein lactylation was observed¹¹⁰. All these data support the argument that lactate may not work only through protein lactylation whether it is histone or any other target. It is likely that lactate could have multiple effects such as HDAC inhibition, maybe context-dependent lactylation of proteins including histones or inhibition of the SENP1 protease. In our model, lactylation is unlikely a major player in OV morphogenesis. However, we cannot exclude the possibility that lactate produced in OVs may increase histone lactylation.

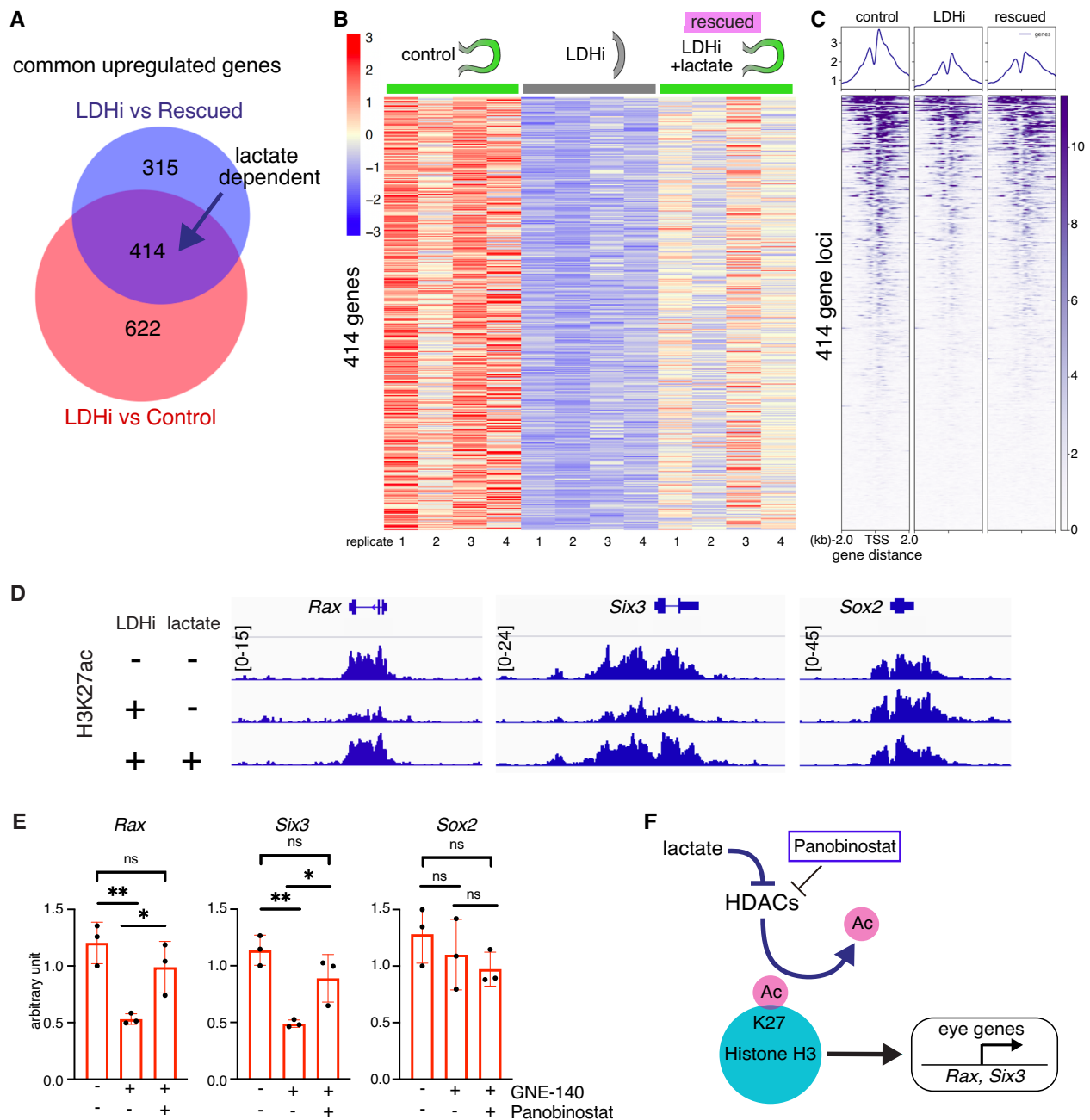


Fig. 6 | HDAC and CBP/p300 activity specifically regulate eye developmental genes. **A** Venn diagram reveals genes whose expression is dependent on lactate. **B** Heatmap of 414 lactate dependent differentially expressed genes. **C** Global histone H3K27 acetylation (H3K27ac) chromatin immunoprecipitation sequencing (ChIPseq) was performed in the following two conditions: 1) addition of the LDH inhibitor (20 μ M), 2) addition of the LDH inhibitor in the presence of lactate (25 mM). The ChIP occupancy heatmaps showing H3K27ac plots at transcription start sites (TSS) (Enhancers/Promoters, \pm 2 kb) of the differentially expressed genes identified from the RNA-seq analysis. **D** Bioinformatic analysis was performed and the ChIPseq data was visualized using the free software IGV (version 2.4.14) around coding and regulatory regions such as putative promoters and/or enhancers of some typical eye gene loci (*Rax*, *Six3*). Relatively higher peaks are seen

in comparison with those upon adding the LDH inhibitor. This peak reduction when adding LDHi was recovered upon lactate treatment. **E** The pan-HDAC inhibitor Panobinostat was added to the organoids in the presence of LDHi from day 4 to day 5. Dual inhibition by LDHi and HDACi rescued eye marker genes at day 5, whereas pan-neural gene, *Sox2* did not change dramatically as seen by qPCR. **F** Potential mechanisms regulating the eye developmental program through H3K27ac involving histone acetyltransferases and deacetylases. Panobinostat, a potent inhibitor depletes histone deacetylases (HDACs) mediated H3K27-deacetylation process. One-way ANOVA followed by Tukey's post-hoc test was performed (**E**). ** $p < 0.01$, * $p < 0.05$, n.s. nonsignificant (**E**). Data are presented as mean values \pm SEM (**E**). Source data are provided as a Source Data file. $n = 3$ biologically independent experiments were performed.

As the last step of glycolysis, the enzymatic activity of LDHA reduces pyruvate into lactate and regenerates NAD^+ from NADH^{49} . The regeneration of cytosolic NAD^+ is required for sustaining cytosolic glucose catabolism by glycolysis^{58,111}. In our RNAseq analysis we identified 414 common genes regulated by LDH and lactate (Fig. 6A). However, the 622 genes listed when comparing control vs LDHi-

treated could certainly be consequence of changes in the NAD^+/NADH ratio. We demonstrated that addition of lactate is sufficient to rescue the process of eye morphogenesis arrested by chemical and genetic ablation of LDH activity (Fig. 5B, E), a result suggesting that NAD^+ is unlikely the major player in this process. In this study, we were able to dissect the critical glycolytic process regulated by lactate-mediated

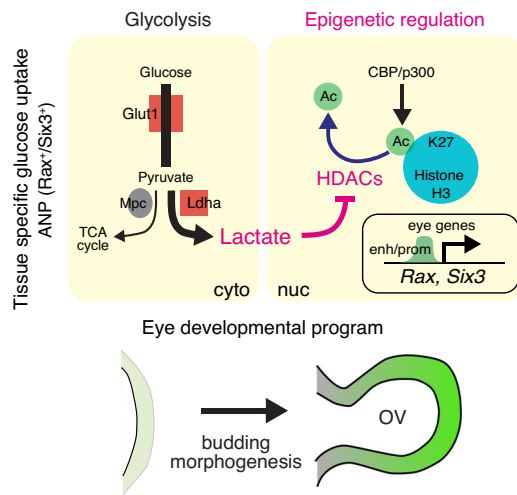


Fig. 7 | Bioenergetics-independent role of lactate during eye morphogenesis. Glycolysis-derived lactate possesses non-metabolic functions that contribute to transcriptional regulation through epigenetic pathways involving histone H3 acetylation writer and eraser. Higher glucose uptake begins in the anterior neural plate (ANP) prior to optic vesicle (OV) morphogenesis. While the activity of *Glut1* and *Ldha* is required for canonical glycolysis, the final product of glycolysis, lactate, acts as a signaling molecule being likely an endogenous HDAC inhibitor during eye morphogenesis. This non-canonical regulation is ATP-production independent and pivotal for specific eye developmental programs. cyto cytoplasm, nuc nucleus, enh enhancers, prom promoters.

transcriptional mechanisms independent from its well-recognized bioenergetic roles.

In summary, glycolysis-derived lactate possesses non-metabolic functions that contribute to transcriptional regulation through epigenetic pathways involving histone H3 acetylation writers and erasers. Higher glucose uptake begins in the anterior neural plate prior to OV morphogenesis. While the activity of *Glut1* and *Ldha* is required for canonical glycolysis, the final product of glycolysis, lactate, acts likely as an endogenous HDAC inhibitor during eye morphogenesis. This non-canonical regulation is ATP-production independent and pivotal for specific eye developmental programs.

Methods

Ethics statement

Our research complies with all relevant ethical regulations and work with mice has been approved by Northwestern University Institutional Animal Care and Use Committee Office.

Optic vesicle differentiation from embryonic stem cells

Mouse embryonic stem cell Rax-EGFP was obtained originally from Dr. Yoshiki Sasai and now is deposited under the name AES0145: Rax-EGFP K/I EBS at RIKEN cell bank. *Rax-EGFP* ESCs were maintained on gelatin-coated dishes in ESC maintenance medium with 2000 U/mL leukemia inhibitory factor (LIF) and 20 μ M blasticidin as described previously³⁹. Cells were passaged every 2–3 days. For differentiation, a standard eye organoid protocol was used¹¹². Briefly, 3000 cells per 100 μ L Glasgow minimum essential medium (GMEM) containing 1.5% knockout serum replacement (KSR) (Life Technologies; called retinal-differentiation medium [RDM]¹¹²; per well were plated in Nunclon Sphera 96-Well, Nunclon Sphera-Treated, U-Shaped-Bottom Microplate (ThermoFisher Scientific, 174929 or 174925) on day 0. On day 1, Matrigel Matrix growth factor reduced (final concentration, 200 μ g/mL) (Corning, 354230) in RDM was added to the aggregates, which were maintained in culture until day 7. Unless stated otherwise, for the pharmacological experiments, 2-Deoxy-D-glucose (2 mM, SIGMA), GNE-140 (20 μ M, SIGMA or MedChemExpress) or UK5099

(1 μ M, MedChemExpress) were added and incubated for 3 days and imaged (EVOS, Cell Imaging System, ThermoFisher), immunostained and analyzed by RT-qPCR (QuantStudio 3, ThermoFisher Scientific). For the rescue experiments, graded methyl-pyruvate (SIGMA)⁶⁶, sodium-L-lactate (25 mM, SIGMA) or eye media with a graded pH (7.8, 7.4, 7.0, 6.6) were added to the eye organoid culture in the presence of 2-Deoxy-D-glucose or GNE-140 for 3 days. The graded pH was prepared prior to the rescue experiment to evaluate the effect of pH in cultured eye organoids. The rationale for this pH range is that it has been shown that extracellular pH (pHe) of -6.6 to -8 is an appropriate physiological range that a cell would encounter in-vivo, and that range is most commonly tested^{113–117}. Supporting the pH range used in this assay, a recent review exploring the range of pH in normal and tumor tissues found that pH is in the same range that we tested in our experiments¹¹⁷. Therefore, the range of pH is consistent with the previous literature and close to the physiologic situation in tissues. The samples were collected for imaging (EVOS), immunostaining and analyzed by RT-qPCR. Panobinostat (0.05 μ M, Selleck Chemicals) and A-485 (2 μ M, MedChemExpress) were added to the culture at differentiation day 4 for a day, followed by gene expression analysis. Embryonic stem cell-qualified fetal bovine serum, KSR and Matrigel Matrix were used for the eye organoid culture.

Single cell RNA sequencing

For preparation of single cells, the eye organoids were collected into 15 mL tubes. Then the tissue was washed with PBS twice and 0.75 mL of warmed Papain (Worthington Biochemical Corporation) was added with DNase I (1:1000, Sigma) and Y-27632 (10 μ M, Millipore) and incubated at 37°C. After 45 min, the tissue was carefully pipetted, and a stop solution was added. The dissociated solution was filtered with a 100 μ m cell strainer (Falcon; Corning) and centrifuged at 1000 rpm at room temperature (RT) for 5 min. 1 mL HBSS (0.2% BSA fraction V + 10 μ M Y-27632) was added to the cell pellets and then filtered using a 40 μ m cell strainer (Falcon; Corning). Cells were counted using a Cellometer K2 (Nexcelom) with acridine orange to calculate total number of nucleated cells and propidium iodide to count dead cells (cell viability was 89%). The library preparation and sequence were performed as described previously¹¹⁸. The single cell organoid samples from three biologically independent experiments were pooled prior to the library generation. Single-cell 3' RNA sequencing libraries were prepared using Chromium Single Cell v2 Reagent Kit and Controller (10X Genomics, Pleasanton, CA, USA). Libraries were assessed for quality (TapeStation 4200; Agilent, Santa Clara, CA, USA) and then sequenced on an HiSeq 4000 instrument (Illumina, San Diego, CA, USA). Raw reads were demultiplexed, filtered, and mapped to the mouse reference genome (mm10) using Cell Ranger 7.0.0 with default settings. The raw feature-barcode matrices generated by Cell Ranger were used for downstream analysis using Seurat v4.1.1. To exclude low-quality cells, standard filters were applied (cells with fewer than 500 genes and higher than 5000 genes) (cells with fewer than 500 UMIs (unique molecular identifiers) and over the 90th quantile of total UMIs (26000) (cells with more than 10% mitochondrial genes) (cells with fewer than 20% ribosomal genes) (cells with higher than 0.5% hemoglobin genes). The cell counts for phase 2 was 9949 cells and for phase 3 7977 cells. The filtered expression data was normalized for each cell by the total expression, multiplied by a scale factor of 10,000, and then log-transformed. The cell-cycle phase scores were calculated for regression. A total of 12792 variable genes were identified. The data was scaled using ScaleData (cell cycle results S.Score and G2M.Score, percentage of mitochondrial genes, number of features, and sample identities were regressed) to remove batch effects. Dimensionality reduction was done using Principal Component Analysis (PCA) and based on the results 50 PCs were used to identify clusters. The clusters were identified using the Approximate Nearest Neighbors

method at different resolutions. After analyzing the different resolutions, 0.2 was chosen for further analysis and 10 clusters were identified. Marker genes were identified using FindAllMarkers (MAST method).

Generation of mutant mouse strains

Six3^{LacZ} mice were previously described⁵⁴. Genotyping was performed using specific primers to identify the WT and *LacZ* null alleles. *Rax* flox mice were kindly provided by Dr. Seth Blackshaw (Johns Hopkins University) and were previously described¹¹⁹. *Rax* flox mice were crossed with *E2a-Cre*¹²⁰ (Jackson lab #003724) kindly provided by Dr. Susan Quaggin (Northwestern University). The F1 animals were genotyped with specific primers to detect germline deletion to obtain the *Rax* KO allele¹¹⁹. *Ldha* flox mice were purchased from Jackson lab (Strain #030112). *Ldha* flox mice were crossed with *E2a-Cre* and F1 animals were genotyped using specific primers to identify the germline delta allele. *Glut1* flox mice were kindly provided by Dr. E. Dale Abel (University of Iowa) and were previously described¹²¹. After cross with *E2a-Cre*, genotyping was performed using specific primers to identify the germline delta allele. *Rax-Cre* mice were previously described⁵⁵. Primers spanning the *Cre* and the *Rax* sequences were used for PCR genotyping. *Rax-Cre* mice were used to generate conditional mice (*Glut1^{flox/delta}; Rax-Cre, Ldha^{flox/delta}; Rax-Cre*); only one flox allele remains upon conditional Cre expression. Embryonic stages were assessed from the day of the vaginal plug that was designated as embryonic day 0.5 (E0.5). Strains are maintained in a mixed C57B6/NMRI background. The embryos were dissected in DMEM and observed under a microscope (Leica). All experimental procedures involving animals in this study were approved by the Institutional Animal Care and Use Committee and Northwestern University. Throughout the study, mice were housed at the Center for Comparative Medicine of Northwestern University (Chicago, IL, USA). Animals were maintained on a standard 12 h lighting cycle in a vivarium maintained at 21–23 °C, relative humidity of 30–70% and received unrestricted access to standard mouse diet (Teklad #7912, Envigo, Indianapolis, IN) and water.

Derivation of conditional *Ldha* null ESCs

The conditional *Ldha* null and heterozygous ESCs were derived as described previously⁴¹. Briefly, irradiated mouse embryonic fibroblasts (MEFs) feeder cells were seeded prior to the isolation of blastocysts (E3.5). Isolated E3.5 embryos were transferred to MEFs in a conventional ESC maintenance medium¹²² supplemented with R2i (two chemical inhibitors, 10 μM SB431542 and 1 μM PD0325901). Typically, embryos were well-adhered to the culture dish with MEFs and hatched in 2 days. On day-7, dissociation into single cells was performed using TrypLE Express Enzyme when outgrowth of the inner cell mass (ICM) became evident. Cells were then continuously cultured in the ESC maintenance medium now supplemented with 2i (two chemical inhibitors, 3 μM CHIR99021 and 1 μM PD0325901) in the presence of MEFs. Optionally, the addition of Y-27632 (10 μM) for the first 2 days improved cell survival after single cell dissociation. Genotyping of each ESC line was performed after the complete removal of MEFs in a non-feeder culture. Primer sequences for genotyping: *Ldha* flox and wild-type alleles, *Ldha*-F 33676, 5'- CTGAGCACACCCATGTGAGA-3'; *Ldha*-R 33677, 5'- AGCAACTCCAAGTCAGGA-3'; *Ldha* delta allele, *Ldha*-F 33676, 5'- CTGAGCACACCCATGTGAGA -3'; *Ldha*-R2 delta, 5'- AGTG TCTTCTCTCCCTCAC -3'. *Rax-Cre* allele, *Rax-Cre*-F, 5'- AGATGCC AGGACATCAGGAACCTG-3'; *Rax-Cre*-R, 5'- ATCAGCCACACCAGACAC AGAGATC -3'. Pluripotency of each clone was initially evaluated by alkaline phosphatase staining and immunostaining by combinations of embryonic stem cell markers. Cells were passaged every 3 days for ESC maintenance. For the eye organoid differentiation protocol, MEFs were removed from the 0.1% (wt/vol) gelatin-coated dish to isolate floating ESCs alone. The standard protocol was used to perform SFEBq

(serum-free floating culture of embryoid body-like aggregates with quick aggregation) in Nunclon Sphera 96-Well, Nunclon Sphera-Treated, U-Shaped-Bottom Microplate (ThermoFisher Scientific, 174929 or 174925) on day 0. On day 1, Matrigel Matrix growth factor reduced (final concentration 100 μg/mL) (Corning, 354230) was added to the aggregates in retina differentiation medium³⁹. Embryonic stem cell-qualified fetal bovine serum, KSR and Matrigel Matrix were used for the eye organoid culture.

Glucose uptake imaging of mouse embryos

Imaging glucose uptake in mouse embryos was performed as described previously^{21,22}. Briefly, freshly dissected E8.0 or E8.5 embryos were washed twice with a glucose blank medium (Thermo, A14430-01) and then incubated in RDM containing 2-NBDG at a final concentration of 0.5 mM (ThermoFisher Scientific, N13195) for 1 h (37°C and 60% O₂, 5% CO₂). Embryos were washed with the medium 3 times for 30 min in total. Imaging was performed under a fluorescent microscope (EVOS) and analyzed by ImageJ (NIH). 2-NBDG uptake in the anterior neural plate was quantified relative to heart tissues.

Immunohistochemistry

Standard protocols for embryo isolation^{41,71} were used. Briefly, embryos for immunohistochemistry were dissected in PBS and fixed in 4% paraformaldehyde in 0.1 M PBS (pH 7.4). After overnight protection in 30% sucrose/PBS, tissues were embedded in sucrose:OCT (Tissue-Tek) and sectioned in a cryostat. The following antibodies were used: anti-Rax (1:1000; TaKaRa, M229), anti-GFP (1:1000; Abcam, ab13970), Laminin (1:1000, Sigma-Aldrich, L9393), anti-Six3 (1:1000, custom made, Rockland), anti-Lhx5 (1:250, R&D systems, AF6290), anti-active Caspase-3 (1:500; BD Pharmingen, 559565), Cre (1:500; Chemicon, MAB3120, clone 2D8) and LDHA (1:500; Abcam, ab47010). The following secondary antibodies were used: Alexa 488-conjugated goat anti-chicken (1:1000, A11039, Invitrogen), Alexa 488-conjugated donkey anti-rabbit (1:1000, A-21206, Invitrogen), Alexa 488-conjugated donkey anti-goat (1:1000, A-11055, Invitrogen), Cy3-conjugated donkey anti-rabbit (1:200, 711-165-152, Jackson ImmunoResearch), Cy3-conjugated donkey anti-mouse (1:200, 715-165-151, Jackson ImmunoResearch), Cy3-conjugated donkey anti-goat (1:200, 705-165-147, Jackson ImmunoResearch), Cy5-conjugated donkey anti-goat (1:200, 705-495-147, Jackson ImmunoResearch), Jackson ImmunoResearch), Cy5-conjugated donkey anti-rabbit (1:200, 711-495-152, Jackson ImmunoResearch). CY5-conjugated goat anti-Guinea Pig (1:200, Jackson 106-175-003, Jackson ImmunoResearch). DAPI (1:1000) was used for DNA. Phalloidin was used to detect F-Actin. Images were obtained in a Zeiss AxioScope and analyzed by ImageJ (NIH).

Quantitative PCR

As previously described⁴¹, the eye organoids were harvested at different days of differentiation and mRNA was isolated using RNeasy Mini Kit (QIAGEN). cDNA was generated (Clontech Laboratories) and 20 ng was used for qRT-PCR amplification using SYBR green. Primer sequences used in this study: *Gapdh*, forward, 5'-GGCATTGCTC TCAATGACAA-3'; reverse, 5'- CCCTGTTGCTGTAGCCGTAT-3'; *Six3*, forward, 5'-TCAGCAGAGTCACCGTCCAC-3'; reverse, 5'- TACCGAGA GGATCGAAGTGC-3'; *Rax*, forward, 5'-CGACGTTCCACCACTTACCAA-3'; reverse, 5'- TCGGTTCTGGAACCATACCT-3'; *Pax6*, forward, 5'-CAAAC AACCTGCCTATGCAA-3'; reverse, 5'- GGCAGCATGCACGAGTATGA-3'; *Lhx2*, forward, 5'- CAGCTTGCGCAAAAGACC -3'; reverse, 5'- TAAAA GGTTGCGCCTGAACT -3'. *Sox2*, forward, 5'- AACTTTTGTCCGAGACCG AGAA -3'; reverse, 5'- CCTCCGGGAAGCGTGTACT -3'; *Ldha*, forward, 5'- GGCAGTACGCGAGACAAG -3'; reverse, 5'- TGATCACCTCGTAGG CACTG -3'. *Gapdh* was used as a housekeeping gene (i.e., its expression was used to normalize gene expression levels). The relative level of each gene was calculated using the 2^{-ΔΔCt} method and reported as relative fold-change mean ± S.E.M.

Glucose and lactate isotope labeling

For glucose or lactate labeling^{61,123}, glucose-free RPMI medium was supplemented with 10% dialyzed FBS and U¹³C-glucose (2 g/liter; Cambridge Isotope Laboratories) or U¹³C-lactate (2 g/liter; Cambridge Isotope Laboratories). All the organoids (50 organoids per condition) were washed with blank SILAC before being reconstituted in ¹³C medium at a concentration of 10 eye organoids/ml. The incubation was performed from 15 min to 2 h for time-course analysis of glucose flux. For the analysis in Fig. 4G and Supplementary Fig. 4, LDH inhibitor (GNE-140) treatment was done 30 min prior to the isotopic labeling experiments and the treatment continued until sample collection (¹³C labeling time was 30 min). The eye organoids were collected and washed twice with PBS before pellets were flash-frozen and stored at -80 °C until metabolite extraction. Metabolite analysis was performed as described previously¹²⁴. Briefly, for metabolite extraction, 80% methanol was used followed by the rapid freeze-thaw method to break the tissues. The supernatant underwent speedvac drying. The samples were prepared in 80% acetonitrile and were analyzed by High-Resolution Liquid Chromatography Tandem Mass Spectrometry (LC-MS/MS). To control for the same concentration of protein/metabolites used as input for LC-MS/MS, we performed a series of controls as follows: 1. The same number of organoids are used for metabolite extraction; 2. When metabolite levels were analyzed, all data were normalized to total ion count/chromatogram (TIC)¹²⁵; 3. When labeling data was analyzed, all isotopic enrichment for each metabolite were calculated against the total pool of unlabeled for each metabolite. For analyzing ¹³C-glucose labeling, the standard % enrichment (fractional enrichment displayed as percentages) was calculated using the normalized peak area of each metabolite's isotopologue over its total pool as described in ref. 126. All data including TIC and unlabeled pools for each metabolite is available upon request.

Extracellular acidification and oxygen consumption rate measurements

Extracellular acidification rate (ECAR) and oxygen consumption rate (OCR) were measured using an XF96 extracellular flux analyzer (Seahorse Bioscience) as previously described^{124,127}. XF96 cell culture plates were coated with Cell-Tak (Corning, Cat. # 354240) to enhance immobilization of samples at the bottom. Typically, one eye organoid contains 10 thousand cells. The organoids were washed and resuspended with Seahorse XF base medium without phenol red (Agilent, Cat# 103335-100) supplemented with L-Glutamine (2 mM; Millipore Sigma, Cat. #G8540). Five to eight organoids per well were plated onto the XF96 plates and spun down at 400 × g for 2 min without deceleration. Prior to performing the assay, plates were incubated at 37°C without CO₂. First, 10 mM glucose or lactate were injected to the seahorse microplates. After three initial readings, oligomycin (2 μM; Agilent, Cat. #103015-100) was injected into each well. Next, to monitor glycolytic activity, 2-DG (25 mM) or GNE-140 (20 μM) were added to the plate followed by three readings to complete ECAR and OCR tracing.

RNA sequencing

The eye organoids were harvested (four biological independent experiments) and total RNA was isolated using RNeasy Mini Kit (QIAGEN). Prior to the library preparation, RNA quantification was performed by Qubit (Thermo Fisher). Next, a high sensitivity RNA assay was used to determine the quality of total RNA (bioanalyzer, Agilent Technologies). TruSeq mRNA-Seq Library Prep was performed, and the libraries were sequenced by Illumina HiSeq 4000 (50 bp, Single-Read, 300 million Reads) in the sequencing core at Northwestern University. Bioinformatic analysis generated Heatmap and Venn diagrams. The genes are ordered or sorted by log fold change to split them into upregulated and downregulated sets. The significant genes that had an FDR-adjusted *p*-value < 0.05 as thresholds/cutoffs were

included in the Venn diagram generated using BioVenn¹²⁸. The RNA-seq gene expression heatmaps were created with R version 3.3.1.

ChIP sequencing

ChIP was performed as described previously¹²⁹. Briefly, 100 eye organoids per experiment were harvested and crosslinked adding 1% formaldehyde/PBS in suspension for 20 min at RT on a rocker and quenched using 125 mM Glycine. The organoids were spun down and snap-frozen in liquid nitrogen. 300 organoids from three biologically independent experiments were pooled per treatment condition. This study performed two sets of ChIP sequencing from six biologically independent experiments. The samples were sonicated using a Covaris E220 system. Sonication conditions were 20% duty factor for histones, peak intensity pulse 140, and 200 cycles per burst for 4 min. Detergent compatible (DC) protein assay (Bio-Rad Laboratories) for protein quantification were performed to normalize each sample. Anti-Acetyl-Histone H3 (Lys27) (1:50, Cell Signaling technology, #8173S) was used for chromatin precipitation overnight on a rotator at 4°C. Chromatin immunoprecipitated DNA purification was done using ChIP DNA Clean & Concentrator (ZYMO RESEARCH, D5205). Prior to the library preparation, high sensitivity DNA assay was used to determine the quality of total DNA (bioanalyzer, Agilent Technologies). DNA-Seq library preparation was performed, and the libraries were sequenced by Illumina HiSeq 4000 (50 bp, Single-Read, 300 million Reads) in the sequencing core at Northwestern University. Bioinformatic analysis generated Annotated Peaks and Bigwig files. The command for Peak calling parameters using sample Kac_control as an example is: findPeaks Kac_control -style histone -o auto -i Input &> Kac_control_findPeaks.log. For data quality, Peaks at FDR 5% and above 5-fold enrichment were used as follows: H3K27ac_control (825105), H3K27ac_LDHi (1056232), H3K27ac_rescue (1036266). The data was visualized by a software, IGV_2.4.14 (Integrative Genomics Viewer, Broad Institute). The occupancy heatmaps (ChIP-seq) were created using deepTools version 2.5.4.

Statistics & reproducibility

All experiments were independently performed at least 3 times except for the metabolomics analysis in Fig. 4B, as another time point (e.g., 60 min) shows a similar trend of isotopic labeling after it reaches a steady state. No data were excluded from the analyses. Representative micrographs are shown, as similar results were obtained from independent replicas. Values are expressed as mean ± S.E.M (standard error of the mean). Results were analyzed using GraphPad (GraphPad version 9.5.1) and Microsoft Excel. For statistical significance test, Student's *t* test and one-way ANOVA were used for two-group and multiple-group comparison, respectively. In addition, post-hoc Tukey's (all groups) or Dunnett's test (versus control) was applied to compare multiple groups. Differences with *p*-value < 0.05 were considered statistically significant. *, ** or *** indicates a *p*-value is less than 0.05, 0.01 or 0.001, respectively. ns non-significance.

Reporting summary

Further information on research design is available in the Nature Portfolio Reporting Summary linked to this article.

Data availability

The materials used in this study are available upon request. The scRNAseq, RNAseq and ChIPseq omics data is compiled under GEO accession number GSE202759. The metabolomics data in this study is available at the NIH Common Fund's National Metabolomics Data Repository (NMDR) website, the Metabolomics Workbench, <https://www.metabolomicsworkbench.org> where it has been assigned Project ID PRO01619. The data can be accessed directly via it's Project <https://doi.org/10.21228/M8F41P>. Source data are provided with this paper.

References

- Warburg, O. On respiratory impairment in cancer cells. *Science* **124**, 269–270 (1956).
- Warburg, O. On the origin of cancer cells. *Science* **123**, 309–314 (1956).
- Warburg, O., Wind, F. & Negelein, E. The metabolism of tumors in the body. *J. Gen. Physiol.* **8**, 519–530 (1927).
- Vander Heiden, M. G., Cantley, L. C. & Thompson, C. B. Understanding the Warburg effect: the metabolic requirements of cell proliferation. *Science* **324**, 1029–1033 (2009).
- Hurley, J. B., Lindsay, K. J. & Du, J. Glucose, lactate, and shuttling of metabolites in vertebrate retinas. *J. Neurosci. Res* **93**, 1079–1092 (2015).
- Ames, A. CNS energy metabolism as related to function. *Brain Res. Rev.* **34**, 42–68 (2000).
- Chinchore, Y., Begaj, T., Wu, D., Drokhlyansky, E. & Cepko, C. L. Glycolytic reliance promotes anabolism in photoreceptors. *Elife* **6**, e25946 (2017).
- Petit, L. et al. Aerobic glycolysis is essential for normal rod function and controls secondary cone death in retinitis pigmentosa. *Cell Rep.* **23**, 2629–2642 (2018).
- Bramall, A. N., Wright, A. F., Jacobson, S. G. & McInnes, R. R. The genomic, biochemical, and cellular responses of the retina in inherited photoreceptor degenerations and prospects for the treatment of these disorders. *Annu Rev. Neurosci.* **33**, 441–472 (2010).
- Punzo, C., Kornacker, K. & Cepko, C. L. Stimulation of the insulin/mTOR pathway delays cone death in a mouse model of retinitis pigmentosa. *Nat. Neurosci.* **12**, 44–52 (2009).
- Zhang, L. et al. Reprogramming metabolism by targeting sirtuin 6 attenuates retinal degeneration. *J. Clin. Invest.* **126**, 4659–4673 (2016).
- Ames, A., Li, Y. Y., Heher, E. C. & Kimble, C. R. Energy-metabolism of rabbit retina as related to function - high cost of Na⁺ transport. *J. Neurosci.* **12**, 840–853 (1992).
- Grenell, A. et al. Loss of MPC1 reprograms retinal metabolism to impair visual function. *Proc. Natl Acad. Sci. USA* **116**, 3530–3535 (2019).
- Agathocleous, M. et al. Metabolic differentiation in the embryonic retina. *Nat. Cell Biol.* **14**, 859–864 (2012).
- Fiske, B. P. & Vander Heiden, M. G. Seeing the Warburg effect in the developing retina. *Nat. Cell Biol.* **14**, 790–791 (2012).
- Shyh-Chang, N., Daley, G. Q. & Cantley, L. C. Stem cell metabolism in tissue development and aging. *Development* **140**, 2535–2547 (2013).
- Schell, J. C. et al. Control of intestinal stem cell function and proliferation by mitochondrial pyruvate metabolism. *Nat. Cell Biol.* **19**, 1027–1036 (2017).
- Solomonson, A. et al. Compartmentalized metabolism supports midgestation mammalian development. *Nature* **604**, 349–353 (2022).
- Flores, A. et al. Lactate dehydrogenase activity drives hair follicle stem cell activation. *Nat. Cell Biol.* **19**, 1017–1026 (2017).
- Snaebjornsson, M. T. & Schulze, A. Non-canonical functions of enzymes facilitate cross-talk between cell metabolic and regulatory pathways. *Exp. Mol. Med.* **50**, 1–16 (2018).
- Oginuma, M. et al. A gradient of glycolytic activity coordinates FGF and Wnt signaling during elongation of the body axis in amniote embryos. *Dev. Cell* **40**, 342–353 e310 (2017).
- Bulusu, V. et al. Spatiotemporal analysis of a glycolytic activity gradient linked to mouse embryo mesoderm development. *Dev. Cell* **40**, 331–341 e334 (2017).
- Oginuma, M. et al. Intracellular pH controls WNT downstream of glycolysis in amniote embryos. *Nature* **584**, 98–101 (2020).
- Zhang, D. et al. Metabolic regulation of gene expression by histone lactylation. *Nature* **574**, 575–580 (2019).
- Moreno-Yruela, C. et al. Class I histone deacetylases (HDAC1-3) are histone lysine delactylases. *Sci. Adv.* **8**, eabi6696 (2022).
- Pan, R. Y. et al. Positive feedback regulation of microglial glucose metabolism by histone H4 lysine 12 lactylation in Alzheimer's disease. *Cell Metab.* **34**, 634–648.e6 (2022).
- Li, L. et al. Glis1 facilitates induction of pluripotency via an epigenome-metabolome-epigenome signalling cascade. *Nat. Metab.* **2**, 882–892 (2020).
- Yu, J. et al. Histone lactylation drives oncogenesis by facilitating m(6)A reader protein YTHDF2 expression in ocular melanoma. *Genome Biol.* **22**, 85 (2021).
- Irizarry-Caro, R. A. et al. TLR signaling adapter BCAP regulates inflammatory to reparatory macrophage transition by promoting histone lactylation. *Proc. Natl Acad. Sci. USA* **117**, 30628–30638 (2020).
- Hagihara, H. et al. Protein lactylation induced by neural excitation. *Cell Rep.* **37**, 109820 (2021).
- Dai, X., Lv, X., Thompson, E. W. & Ostrikov, K. K. Histone lactylation: epigenetic mark of glycolytic switch. *Trends Genet.* **38**, 124–127 (2022).
- Liberti, M. V. & Locasale, J. W. Histone lactylation: a new role for glucose metabolism. *Trends Biochem. Sci.* **45**, 179–182 (2020).
- O'Hara-Wright, M. & Gonzalez-Cordero, A. Retinal organoids: a window into human retinal development. *Development* **147**, dev189746 (2020).
- Fuhrmann, S. Eye morphogenesis and patterning of the optic vesicle. *Curr. Top. Dev. Biol.* **93**, 61–84 (2010).
- Martinez-Morales, J. R. & Wittbrodt, J. Shaping the vertebrate eye. *Curr. Opin. Genet. Dev.* **19**, 511–517 (2009).
- Guillot, C. & Lecuit, T. Mechanics of epithelial tissue homeostasis and morphogenesis. *Science* **340**, 1185–1189 (2013).
- Rozario, T. & DeSimone, D. W. The extracellular matrix in development and morphogenesis: a dynamic view. *Dev. Biol.* **341**, 126–140 (2010).
- Kim, H. Y. & Nelson, C. M. Extracellular matrix and cytoskeletal dynamics during branching morphogenesis. *Organogenesis* **8**, 56–64 (2012).
- Eiraku, M. et al. Self-organizing optic-cup morphogenesis in three-dimensional culture. *Nature* **472**, 51–56 (2011).
- Nakano, T. et al. Self-formation of optic cups and storable stratified neural retina from human ESCs. *Cell Stem Cell* **10**, 771–785 (2012).
- Takata, N. et al. An eye organoid approach identifies Six3 suppression of R-spondin 2 as a critical step in mouse neuroretina differentiation. *Cell Rep.* **21**, 1534–1549 (2017).
- Diacou, R. et al. Cell fate decisions, transcription factors and signaling during early retinal development. *Prog. Retin Eye Res.* **91**, 101093 (2022).
- Pijuan-Sala, B. et al. A single-cell molecular map of mouse gastrulation and early organogenesis. *Nature* **566**, 490–495 (2019).
- Ibarra-Soria, X. et al. Defining murine organogenesis at single-cell resolution reveals a role for the leukotriene pathway in regulating blood progenitor formation. *Nat. Cell Biol.* **20**, 127–134 (2018).
- Ida-Yonemochi, H. et al. Glucose uptake mediated by glucose transporter 1 is essential for early tooth morphogenesis and size determination of murine molars. *Dev. Biol.* **363**, 52–61 (2012).
- Zhang, S. L. et al. Reactive oxygen species in the presence of high glucose alter ureteric bud morphogenesis. *J. Am. Soc. Nephrol.* **18**, 2105–2115 (2007).
- Schmidt, S. et al. Essential role of glucose transporter GLUT3 for post-implantation embryonic development. *J. Endocrinol.* **200**, 23–33 (2009).

48. Heilig, C. W. et al. Glucose transporter-1-deficient mice exhibit impaired development and deformities that are similar to diabetic embryopathy. *Proc. Natl Acad. Sci. USA* **100**, 15613–15618 (2003).
49. Bui, T. & Thompson, C. B. Cancer's sweet tooth. *Cancer Cell* **9**, 419–420 (2006).
50. Boudreau, A. et al. Metabolic plasticity underpins innate and acquired resistance to LDHA inhibition. *Nat. Chem. Biol.* **12**, 779–786 (2016).
51. Miyazawa, H., Yamamoto, M., Yamaguchi, Y. & Miura, M. Mammalian embryos show metabolic plasticity toward the surrounding environment during neural tube closure. *Genes Cells* **23**, 794–802 (2018).
52. Wang, D. et al. A mouse model for Glut-1 haploinsufficiency. *Hum. Mol. Genet.* **15**, 1169–1179 (2006).
53. Mathers, P. H., Grinberg, A., Mahon, K. A. & Jamrich, M. The Rx homeobox gene is essential for vertebrate eye development. *Nature* **387**, 603–607 (1997).
54. Lagutin, O. V. et al. Six3 repression of Wnt signaling in the anterior neuroectoderm is essential for vertebrate forebrain development. *Genes Dev.* **17**, 368–379 (2003).
55. Swindell, E. C. et al. Rx-Cre, a tool for inactivation of gene expression in the developing retina. *Genesis* **44**, 361–363 (2006).
56. Sheng, H. Z. et al. Expression of murine Lhx5 suggests a role in specifying the forebrain. *Dev. Dyn.* **208**, 266–277 (1997).
57. Fernandes-Silva, H. et al. Lung branching morphogenesis is accompanied by temporal metabolic changes towards a glycolytic preference. *Cell Biosci.* **11**, 134 (2021).
58. Merkle, S., Favor, J., Graw, J., Hornhardt, S. & Pretsch, W. Hereditary lactate dehydrogenase A-subunit deficiency as cause of early postimplantation death of homozygotes in *Mus musculus*. *Genetics* **131**, 413–421 (1992).
59. Chandel, N. S. Glycolysis. *Cold Spring Harb. Perspect. Biol.* **13**, a040568 (2021).
60. Yuan, J., Bennett, B. D. & Rabinowitz, J. D. Kinetic flux profiling for quantitation of cellular metabolic fluxes. *Nat. Protoc.* **3**, 1328–1340 (2008).
61. Antoniewicz, M. R. A guide to (13)C metabolic flux analysis for the cancer biologist. *Exp. Mol. Med.* **50**, 1–13 (2018).
62. Yuan, M. et al. Ex vivo and in vivo stable isotope labelling of central carbon metabolism and related pathways with analysis by LC-MS/MS. *Nat. Protoc.* **14**, 313–330 (2019).
63. Halestrap, A. P. The mitochondrial pyruvate carrier. Kinetics and specificity for substrates and inhibitors. *Biochem. J.* **148**, 85–96 (1975).
64. Felig, P. The glucose-alanine cycle. *Metabolism* **22**, 179–207 (1973).
65. Farhana, A. & Lappin, S. L. Biochemistry, Lactate Dehydrogenase. in *StatPearls [Internet]* (StatPearls Publishing, Treasure Island (FL), 2023).
66. Lambert, N., Joos, H. C., Idahl, L. A., Ammon, H. P. T. & Wahl, M. A. Methyl pyruvate initiates membrane depolarization and insulin release by metabolic factors other than ATP. *Biochem. J.* **354**, 345–350 (2001).
67. Michl, J., Park, K. C. & Swietach, P. Evidence-based guidelines for controlling pH in mammalian live-cell culture systems. *Commun. Biol.* **2**, 144 (2019).
68. Ivashkiv, L. B. The hypoxia-lactate axis tempers inflammation. *Nat. Rev. Immunol.* **20**, 85–86 (2020).
69. Haas, R. et al. Intermediates of metabolism: from bystanders to signalling molecules. *Trends Biochem. Sci.* **41**, 460–471 (2016).
70. Certo, M., Marone, G., de Paulis, A., Mauro, C. & Pucino, V. Lactate: fueling the fire starter. *Wiley Interdiscip. Rev. Syst. Biol. Med* **12**, e1474 (2020).
71. Liu, W., Lagutin, O., Swindell, E., Jamrich, M. & Oliver, G. Neuronal specification in mouse embryos requires Six3-mediated suppression of Wnt8b in the anterior neural plate. *J. Clin. Invest.* **120**, 3568–3577 (2010).
72. Burns, C. J. et al. Investigation of Frizzled-5 during embryonic neural development in mouse. *Dev. Dyn.* **237**, 1614–1626 (2008).
73. Yamamoto, A., Nagano, T., Takehara, S., Hibi, M. & Aizawa, S. Shisa promotes head formation through the inhibition of receptor protein maturation for the caudalizing factors, Wnt and FGF. *Cell* **120**, 223–235 (2005).
74. Behesti, H., Papaioannou, V. E. & Sowden, J. C. Loss of Tbx2 delays optic vesicle invagination leading to small optic cups. *Dev. Biol.* **333**, 360–372 (2009).
75. Sanyanusin, P. et al. Mutation of the PAX2 gene in a family with optic nerve colobomas, renal anomalies and vesicoureteral reflux. *Nat. Genet.* **9**, 358–364 (1995).
76. Torres, M., Gomez-Pardo, E. & Gruss, P. Pax2 contributes to inner ear patterning and optic nerve trajectory. *Development* **122**, 3381–3391 (1996).
77. Babcock, H. E. et al. aldh7a1 regulates eye and limb development in zebrafish. *PLoS One* **9**, e101782 (2014).
78. Flach, H. et al. Retinol binding protein 1 affects *Xenopus* anterior neural development via all-trans retinoic acid signaling. *Dev. Dyn.* **250**, 1096–1112 (2021).
79. Hanel, M. L. & Hensey, C. Eye and neural defects associated with loss of GDF6. *BMC Dev. Biol.* **6**, 43 (2006).
80. Capowski, E. E. et al. Loss of MITF expression during human embryonic stem cell differentiation disrupts retinal pigment epithelium development and optic vesicle cell proliferation. *Hum. Mol. Genet.* **23**, 6332–6344 (2014).
81. Koshiba-Takeuchi, K. et al. Tbx5 and the retinotectum projection. *Science* **287**, 134–137 (2000).
82. Barbieri, A. M. et al. A homeobox gene, *vax2*, controls the patterning of the eye dorsoventral axis. *Proc. Natl Acad. Sci. USA* **96**, 10729–10734 (1999).
83. Hasegawa, Y. et al. Emergence of dorsal-ventral polarity in ESC-derived retinal tissue. *Development* **143**, 3895–3906 (2016).
84. Gamm, D. M., Clark, E., Capowski, E. E. & Singh, R. The role of FGF9 in the production of neural retina and RPE in a pluripotent stem cell model of early human retinal development. *Am. J. Ophthalmol.* **206**, 113–131 (2019).
85. Dai, Z., Ramesh, V. & Locasale, J. W. The evolving metabolic landscape of chromatin biology and epigenetics. *Nat. Rev. Genet.* **21**, 737–753 (2020).
86. Chakrabarty, R. P. & Chandel, N. S. Mitochondria as signaling organelles control mammalian stem cell fate. *Cell Stem Cell* **28**, 394–408 (2021).
87. Morgan, M. A. J. & Shilatifard, A. Reevaluating the roles of histone-modifying enzymes and their associated chromatin modifications in transcriptional regulation. *Nat. Genet.* **52**, 1271–1281 (2020).
88. Ogryzko, V. V., Schiltz, R. L., Russanova, V., Howard, B. H. & Nakatani, Y. The transcriptional coactivators p300 and CBP are histone acetyltransferases. *Cell* **87**, 953–959 (1996).
89. Bannister, A. J. & Kouzarides, T. The CBP co-activator is a histone acetyltransferase. *Nature* **384**, 641–643 (1996).
90. Narita, T. et al. Enhancers are activated by p300/CBP activity-dependent PIC assembly, RNAPII recruitment, and pause release. *Mol. Cell* **81**, 2166–2182 e2166 (2021).
91. Weinert, B. T. et al. Time-resolved analysis reveals rapid dynamics and broad scope of the CBP/p300 acetylome. *Cell* **174**, 231–244 e212 (2018).
92. Bedford, D. C., Kasper, L. H., Fukuyama, T. & Brindle, P. K. Target gene context influences the transcriptional requirement for the KAT3 family of CBP and p300 histone acetyltransferases. *Epigenetics* **5**, 9–15 (2010).

93. Yao, T. P. et al. Gene dosage-dependent embryonic development and proliferation defects in mice lacking the transcriptional integrator p300. *Cell* **93**, 361–372 (1998).
94. Raeisossadati, R., Ferrari, M. F. R., Kihara, A. H., AlDiri, I. & Gross, J. M. Epigenetic regulation of retinal development. *Epigenetics Chromatin* **14**, 11 (2021).
95. Hennig, A. K., Peng, G. H. & Chen, S. Transcription coactivators p300 and CBP are necessary for photoreceptor-specific chromatin organization and gene expression. *PLoS One* **8**, e69721 (2013).
96. Wolf, L. et al. Histone posttranslational modifications and cell fate determination: lens induction requires the lysine acetyltransferases CBP and p300. *Nucleic Acids Res.* **41**, 10199–10214 (2013).
97. Lagger, G. et al. Essential function of histone deacetylase 1 in proliferation control and CDK inhibitor repression. *EMBO J.* **21**, 2672–2681 (2002).
98. Hagelkruys, A. et al. A single allele of Hdac2 but not Hdac1 is sufficient for normal mouse brain development in the absence of its paralog. *Development* **141**, 604–616 (2014).
99. Montgomery, R. L. et al. Maintenance of cardiac energy metabolism by histone deacetylase 3 in mice. *J. Clin. Invest.* **118**, 3588–3597 (2008).
100. Latham, T. et al. Lactate, a product of glycolytic metabolism, inhibits histone deacetylase activity and promotes changes in gene expression. *Nucleic Acids Res.* **40**, 4794–4803 (2012).
101. Bradner, J. E. et al. Chemical phylogenetics of histone deacetylases. *Nat. Chem. Biol.* **6**, 238–243 (2010).
102. Grasso, C. S. et al. Functionally defined therapeutic targets in diffuse intrinsic pontine glioma. *Nat. Med.* **21**, 555–559 (2015).
103. Baker, S. A. & Rutter, J. Metabolites as signalling molecules. *Nat. Rev. Mol. Cell Bio* **24**, 355–374 (2023).
104. Vinaik, R., Barayan, D., Auger, C., Abdullahi, A. & Jeschke, M. G. Regulation of glycolysis and the Warburg effect in wound healing. *JCI Insight* **5**, e138949 (2020).
105. Shyh-Chang, N. et al. Lin28 enhances tissue repair by reprogramming cellular metabolism. *Cell* **155**, 778–792 (2013).
106. Lin, H. et al. Extracellular lactate dehydrogenase A release from damaged neurons drives central nervous system angiogenesis. *EBioMedicine* **27**, 71–85 (2018).
107. Fan, M. et al. Lactate promotes endothelial-to-mesenchymal transition via Snail1 lactylation after myocardial infarction. *Sci. Adv.* **9**, eadc9465 (2023).
108. Wang, N. et al. Histone lactylation boosts reparative gene activation post-myocardial infarction. *Circ. Res.* **131**, 893–908 (2022).
109. Li, F. et al. Glial metabolic rewiring promotes axon regeneration and functional recovery in the central nervous system. *Cell Metab.* **32**, 767–785 e767 (2020).
110. Liu, W. et al. Lactate regulates cell cycle by remodelling the anaphase promoting complex. *Nature* **616**, 790–797 (2023).
111. Yang, Y. & Sauve, A. A. NAD(+) metabolism: bioenergetics, signaling and manipulation for therapy. *Biochim. Biophys. Acta* **1864**, 1787–1800 (2016).
112. Eiraku, M. & Sasai, Y. Mouse embryonic stem cell culture for generation of three-dimensional retinal and cortical tissues. *Nat. Protoc.* **7**, 69–79 (2011).
113. Kondo, A. & Osawa, T. Establishment of an extracellular acidic pH culture system. *J. Vis. Exp.*, 56660, <https://doi.org/10.3791/56660>, (2017).
114. Wu, H. et al. T-cells produce acidic niches in lymph nodes to suppress their own effector functions. *Nat. Commun.* **11**, 4113 (2020).
115. Jiang, W. et al. Extracellular acidity reprograms macrophage metabolism and innate responsiveness. *J. Immunol.* **206**, 3021–3031 (2021).
116. Kellum, J. A., Song, M. & Li, J. Lactic and hydrochloric acids induce different patterns of inflammatory response in LPS-stimulated RAW 264.7 cells. *Am. J. Physiol. Regul. Integr. Comp. Physiol.* **286**, R686–R692 (2004).
117. Steenbergen, C., Deleeuw, G., Rich, T. & Williamson, J. R. Effects of acidosis and ischemia on contractility and intracellular pH of rat heart. *Circ. Res.* **41**, 849–858 (1977).
118. Joshi, N. et al. A spatially restricted fibrotic niche in pulmonary fibrosis is sustained by M-CSF/M-CSFR signalling in monocyte-derived alveolar macrophages. *Eur. Respir. J.* **55**, 1900646 (2020).
119. Voronina, V. A., Kozlov, S., Mathers, P. H. & Lewandoski, M. Conditional alleles for activation and inactivation of the mouse Rx homeobox gene. *Genesis* **41**, 160–164 (2005).
120. Lakso, M. et al. Efficient in vivo manipulation of mouse genomic sequences at the zygote stage. *Proc. Natl Acad. Sci. USA* **93**, 5860–5865 (1996).
121. Fidler, T. P. et al. Deletion of GLUT1 and GLUT3 reveals multiple roles for glucose metabolism in platelet and megakaryocyte function. *Cell Rep.* **20**, 881–894 (2017).
122. Chen, H. Y., Kaya, K. D., Dong, L. & Swaroop, A. Three-dimensional retinal organoids from mouse pluripotent stem cells mimic in vivo development with enhanced stratification and rod photoreceptor differentiation. *Mol. Vis.* **22**, 1077–1094 (2016).
123. Emwas, A. H., Szczepski, K., Al-Younis, I., Lachowicz, J. I. & Jar-emko, M. Fluxomics - new metabolomics approaches to monitor metabolic pathways. *Front. Pharm.* **13**, 805782 (2022).
124. Ma, W. et al. Mitochondrial respiration controls the Prox1-Vegfr3 feedback loop during lymphatic endothelial cell fate specification and maintenance. *Sci. Adv.* **7**, eabe7359 (2021).
125. Mizuno, H. et al. The great importance of normalization of LC-MS data for highly-accurate non-targeted metabolomics. *Biomed. Chromatogr.* **31**, <https://doi.org/10.1002/bmc.3864> (2017).
126. Buescher, J. M. et al. A roadmap for interpreting (13)C metabolite labeling patterns from cells. *Curr. Opin. Biotechnol.* **34**, 189–201 (2015).
127. Pelletier, M., Billingham, L. K., Ramaswamy, M. & Siegel, R. M. Extracellular flux analysis to monitor glycolytic rates and mitochondrial oxygen consumption. *Methods Enzymol.* **542**, 125–149 (2014).
128. Hulsen, T., de Vlieg, J. & Alkema, W. BioVenn - a web application for the comparison and visualization of biological lists using area-proportional Venn diagrams. *BMC Genom.* **9**, 488 (2008).
129. Lee, T. I., Johnstone, S. E. & Young, R. A. Chromatin immunoprecipitation and microarray-based analysis of protein location. *Nat. Protoc.* **1**, 729–748 (2006).

Acknowledgements

Metabolomics services were provided by the Metabolomics Core Facility at the Robert H. Lurie Comprehensive Cancer Center of Northwestern University. The public data deposition is supported by the Metabolomics Workbench/National Metabolomics Data Repository (NMDR) (grant# U2C-DK119886), Common Fund Data Ecosystem (CFDE) (grant# 3OT2OD030544) and Metabolomics Consortium Coordinating Center (M3C) (grant# 1U2C-DK119889). RNA-seq, scRNA-seq and ChIP-seq work were supported by the Northwestern University NUSeq Core Facility. We thank Masayuki Oginuma (Osaka University) and Jun Watanabe (Northwestern University) for technical advice with the glucose tracing experiments and HDAC-mediated epigenetic modification, respectively. Sandra Acosta (University of Barcelona), Beatriz Sosa-Pineda (Northwestern University), Jason S. Shapiro (Northwestern University), Soh Yamamoto (Sapporo Medical University School of Medicine) and Hidenobu Miyazawa (European Molecular Biology Laboratory) for critical

comments. For valuable animal resources, we want to thank E. Dale Abel (University of Iowa), Seth Blackshaw (Johns Hopkins University) and Susan E. Quaggin (Northwestern University). Funding: 2020 Illumina pilot project AAA-Next Generation Sequencing award to G.O.

Author contributions

N.T. and G.O. designed the study. N.S.C provided valuable advice. N.T. and G.O. wrote the manuscript. N.T., J.M.M., L.K.B, P.G. L.P.D., and G.S.M., performed ¹³C metabolic labeling analysis, Seahorse assay and quantifications. N.T., M.A.M., Z.J.D., P.P., R.B.E., and M.J.S., performed ChIPseq and bioinformatic analysis. N.T., N.J., R.B.E., and M.J.S., performed RNAseq and bioinformatic analysis. N.T., N.R.J., A.V.M., P.P., and L.F., performed scRNAseq and data analysis. A. S. provided reagents and technical expertise. N.T. maintained the embryonic stem cell lines and performed the eye organoid culture, generated the standard and conditional null mouse embryos, and performed the conditional mutant organoid assays. All authors reviewed the final manuscript.

Competing interests

The authors declare no competing interests.

Additional information

Supplementary information The online version contains supplementary material available at <https://doi.org/10.1038/s41467-023-39672-2>.

Correspondence and requests for materials should be addressed to Guillermo Oliver.

Peer review information *Nature Communications* thanks the anonymous reviewer(s) for their contribution to the peer review of this work.

Reprints and permissions information is available at <http://www.nature.com/reprints>

Publisher's note Springer Nature remains neutral with regard to jurisdictional claims in published maps and institutional affiliations.

Open Access This article is licensed under a Creative Commons Attribution 4.0 International License, which permits use, sharing, adaptation, distribution and reproduction in any medium or format, as long as you give appropriate credit to the original author(s) and the source, provide a link to the Creative Commons license, and indicate if changes were made. The images or other third party material in this article are included in the article's Creative Commons license, unless indicated otherwise in a credit line to the material. If material is not included in the article's Creative Commons license and your intended use is not permitted by statutory regulation or exceeds the permitted use, you will need to obtain permission directly from the copyright holder. To view a copy of this license, visit <http://creativecommons.org/licenses/by/4.0/>.

© The Author(s) 2023